

RESEARCH ARTICLE

The cell polarity determinant Dlg1 facilitates epithelial invagination by promoting tissue-scale mechanical coordination

Melisa A. Fuentes and Bing He*

ABSTRACT

Epithelial folding mediated by apical constriction serves as a fundamental mechanism to convert flat epithelial sheets into multilayered structures. It remains unknown whether additional mechanical inputs are required for apical constriction-mediated folding. Using *Drosophila* mesoderm invagination as a model, we identified an important role for the non-constricting, lateral mesodermal cells adjacent to the constriction domain ('flanking cells') in facilitating epithelial folding. We found that depletion of the basolateral determinant Dlg1 disrupts the transition between apical constriction and invagination without affecting the rate of apical constriction. Strikingly, the observed delay in invagination is associated with ineffective apical myosin contractions in the flanking cells that lead to overstretching of their apical domain. The defects in the flanking cells impede ventral-directed movement of the lateral ectoderm, suggesting reduced mechanical coupling between tissues. Specifically disrupting the flanking cells in wild-type embryos by laser ablation or optogenetic depletion of cortical actin is sufficient to delay the apical constriction-to-invagination transition. Our findings indicate that effective mesoderm invagination requires intact flanking cells and suggest a role for tissue-scale mechanical coupling during epithelial folding.

KEY WORDS: Apical constriction, Apical-basal polarity, Dlg1, Epithelial folding, Gastrulation, Ventral furrow

INTRODUCTION

Apical constriction is a common mechanism to achieve epithelial folding during tissue morphogenesis (Sawyer et al., 2010). During apical constriction, constricting cell apices shrink and their basal ends expand, resulting in a characteristic wedge-like shape. Such cell shape changes are accompanied by folding of the epithelial sheet into a three-dimensional (3D) tissue. Apical constriction-mediated epithelial folding is a well-conserved process and occurs in a variety of developmental contexts (Nishimura et al., 2012; Leptin and Grunewald, 1990; Sweeton et al., 1991; Sherrard et al., 2010; Kim et al., 2013). Although we have a detailed understanding of how constriction forces are generated near the apical surface of cells (Martin and Goldstein, 2014; Munjal and Lecuit, 2014), it is less well understood how apical forces drive coordinated cell shape changes in the constricting cells and their non-constricting neighbors to transform a flat epithelium into a multilayered structure.

Folding of the prospective mesoderm during *Drosophila* gastrulation provides an excellent model to study epithelial folding. During gastrulation, a subset of ventrally localized mesodermal cells invaginate from the surface of the embryo to form a furrow (Leptin, 1999). Ventral furrow formation completes within 20 min and is characterized by an apical constriction phase and an invagination phase (Sweeton et al., 1991) (Fig. 1A). The presumptive mesoderm is approximately 18 cells wide along the medial-lateral axis. The middle 12 cells that comprise the ventral mesoderm ('constricting mesodermal cells') undergo apical constriction during gastrulation, whereas the three cells flanking each side of the constriction domain that comprise the lateral mesoderm ('flanking cells') do not. During apical constriction, the ventral mesodermal cells constrict apically and elongate in the apical-basal direction ('cell lengthening'). Meanwhile, the constricting mesodermal cells pull the flanking cells towards the ventral midline, causing the flanking cells to become stretched. During subsequent invagination, the constricting mesodermal cells undergo shortening and invaginate inwards to form the ventral furrow ('cell shortening'), whereas the flanking cells remain closer to the surface of the embryo and become the neck of the ventral furrow (Sweeton et al., 1991) (Fig. 1A).

The molecular mechanism that regulates apical accumulation of myosin, and thus apical constriction, in the constricting mesodermal cells has been extensively studied. The expression of two transcription factors, Twist and Snail, at the ventral side of the embryo specifies mesodermal cell fate and promotes ventral furrow formation (Leptin, 1991). Twist and Snail activate the recruitment of RhoGEF2, a Rho GTPase activator, to the apex of the mesodermal precursor cells via a G protein-coupled receptor pathway (Costa et al., 1994; Kerridge et al., 2016; Kölsch et al., 2007; Manning et al., 2013; Parks and Wieschaus, 1991). RhoGEF2 then activates non-muscle myosin II (hereafter 'myosin') across the apical surface of the prospective mesoderm through the Rho-Rho kinase pathway (Barrett et al., 1997; Dawes-Hoang et al., 2005; Häcker and Perrimon, 1998; Martin et al., 2009; Mason et al., 2013; Nikolaidou and Barrett, 2004). Upon activation, myosin forms a contractile actomyosin network that undergoes stochastic, pulsatile contractions, which power constriction of cell apices (Martin and Goldstein, 2014; Martin et al., 2009).

In addition to apical myosin, myosin localized at other subcellular locations in the constricting cells can also influence invagination of the ventral furrow. It has been proposed that proper downregulation of myosin at the basal cortex of the mesodermal cells facilitates tissue internalization by softening the basal membrane (Polyakov et al., 2014). In support of this view, a recent study showed that prolonged retention of basal myosin in the mesodermal cells inhibits ventral furrow invagination (Krueger et al., 2018). In addition, it has been proposed, and recently demonstrated experimentally, that accumulation of myosin along the lateral cortex of the constricting cells facilitates cell shortening

Dartmouth College, Department of Biological Sciences, Hanover, NH 03755, USA.

*Author for correspondence (bing.he@dartmouth.edu)

 B.H., 0000-0002-8564-0933

Handling Editor: Steve Wilson

Received 21 December 2021; Accepted 27 January 2022

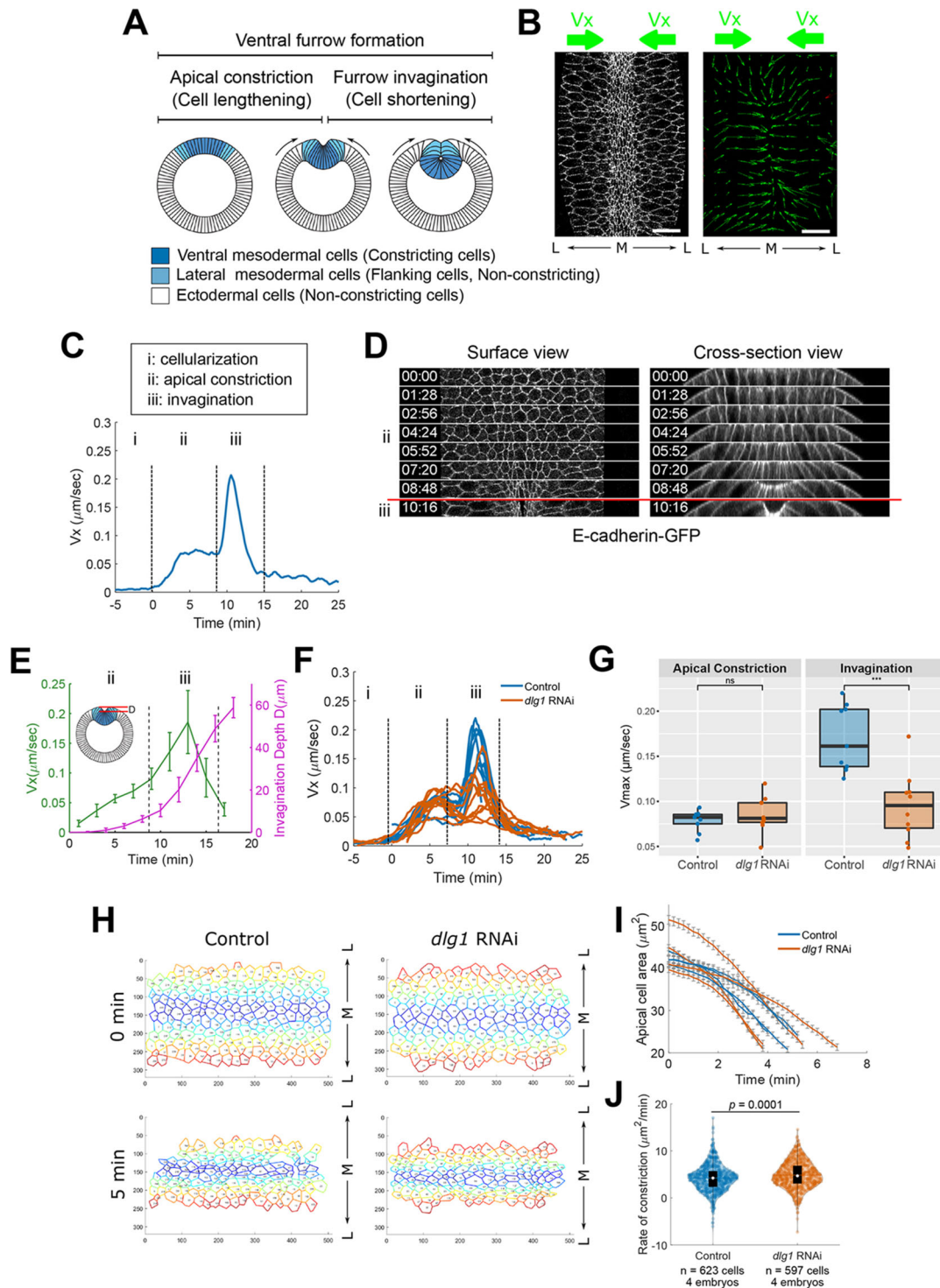


Fig. 1. *dlgl* RNAi embryos undergo normal apical constriction but exhibit slower invagination. (A) Schematic depicting *Drosophila* ventral furrow formation. Arrows indicate tissue flow towards the ventral midline. (B) PIV analysis of tissue movement during ventral furrow formation. A control embryo (left) and its corresponding velocity vectors (right; green arrows) at a single time point are shown as an example. Scale bars: 20 μm . (C) The average velocity of tissue movement (V_x) over time. Time 0 marks the onset of gastrulation throughout the text unless otherwise noted. (D) Movie stills showing surface views and cross-section views of a control embryo undergoing gastrulation. Ventral side is facing up. Red line demarcates T_{trans} . (E) Measurement of V_x and invagination depth in control embryos ($n=8$) imaged on a multiphoton microscope. Error bars represent s.d. (F,G) Maximal V_x during apical constriction and invagination in control and *dlgl* RNAi embryos. For all box and whisker plots, the lower and upper hinges correspond to the first and third quartiles (the 25th and 75th percentiles), the horizontal line indicates the median, and the whiskers indicate the lowest and highest non-outlier values. *** $P \leq 0.001$ (unpaired, two-tailed Student's *t*-test). ns, not significant. (H) The apical domains of the constricting cells were segmented in order to measure the rate of apical constriction. L, lateral; M, medial. (I) Quantification of average cell area reduction in the constriction domain over time in control ($n=4$) and *dlgl* RNAi embryos ($n=4$). Each curve represents one embryo ($n=129$ –164 cells per embryo). Error bars represent s.e.m. (J) Distribution of apical constriction rate in individual cells in control and *dlgl* RNAi embryos. For all violin plots, the lower and upper limits of the black box correspond to the first and third quartiles (the 25th and 75th percentiles), the horizontal line indicates the mean, and the white point in the black box indicates the median.

and furrow invagination (Gracia et al., 2019; John and Rauzi, 2021). Thus, appropriate regulation of myosin contractility in the constricting cells is essential for apical constriction and invagination. Interestingly, a few studies have reported that perturbation of the non-constricting tissues adjacent to the constriction domain, either by upregulation of apical myosin contractility in these cells or by anchoring lateral ectodermal cells to the vitelline membrane, negatively impacts ventral furrow invagination (Fuse et al., 2013; Perez-Mockus et al., 2017; Rauzi et al., 2015). These studies demonstrate that mesoderm invagination can be influenced by the mechanical properties of the surrounding non-constricting tissues. However, the exact mechanical contribution of the non-constricting tissues during ventral furrow formation is currently unknown.

In this work, we found that RNAi-mediated depletion of Dlg1, a protein important for establishing and maintaining apical-basal polarity in epithelial cells, impairs invagination of the ventral furrow without noticeably affecting the constriction domain. Dlg1 helps maintain polarity and basolateral identity by promoting cell junction formation and by preventing basal expansion of apical polarity proteins (Tanentzapf and Tepass, 2003; Woods et al., 1996). During polarity establishment in the *Drosophila* blastoderm, Dlg1 also facilitates the recruitment of apical polarity determinants to the subapical region of the cells (Bonello et al., 2019). We found that knockdown of Dlg1 impairs apical myosin contractions in the flanking cells, causing their apical domain to become overstretched when they are pulled on by the constricting cells. This defect weakens the coupling between the constriction domain and the ectodermal tissue and is associated with a delay in the transition between apical constriction and invagination. A similar delay is observed when the flanking cells are disrupted in wild-type embryos. Together, these results reveal the importance of the flanking cells during ventral furrow formation and suggest that mechanical coupling between the constriction domain and the surrounding ectodermal tissue is required for robust furrow invagination.

RESULTS

Knockdown of Dlg1, a basolateral polarity determinant, impairs the invagination phase of ventral furrow formation without causing obvious defects in apical constriction

Inspired by the observation that apical constriction and invagination are temporally distinct processes during ventral furrow formation (Polyakov et al., 2014; Rauzi et al., 2015), we hypothesized that invagination may have its own unique regulatory inputs separate from those of apical constriction. To search for mutants that are specifically defective in furrow invagination but not in apical constriction, we developed a live imaging-based approach to monitor tissue movement at the surface of the embryo as a readout for the progression of ventral furrow formation (Fig. 1A,B; Materials and Methods). We focused on tissue velocity along the medial-lateral axis (V_x ; 10–30 μm from the ventral midline) because it is the predominant direction of tissue movement at the embryo surface during ventral furrow formation. As expected, we found that there is little cell movement during cellularization ($V_x=0$; Fig. 1C, i). After the onset of apical constriction (which we define as $T=0$ min for the remainder of the text, unless otherwise noted), constriction of the ventral mesodermal cells initiates tissue movement towards the ventral midline, resulting in an increase in V_x that peaks/plateaus approximately 5 min into gastrulation (Fig. 1C, ii). Approximately 8 min after gastrulation onset, there is another rapid increase in V_x that forms a second, more prominent

peak between $T=8$ min and $T=15$ min (Fig. 1C, iii). This rapid increase in V_x temporally correlates with the onset of rapid invagination (Fig. 1D, red line), which we further confirmed by quantifying furrow invagination in deep-tissue live movies (Fig. 1E). Thus, the velocity of tissue flow towards the ventral midline provides a sensitive readout for the progress of ventral furrow formation and reveals the rate of tissue flow during different phases of furrow formation.

Using this approach, we examined embryos containing maternally loaded short hairpin RNAs to silence the expression of specific candidate genes important for epithelial polarity and cell-cell adhesion (*baz*, *aPKC*, *par-6*, *crb*, *sdt*, *dlg1*, *scrib*, *lgl*, *shg*, *Vang*) (Ni et al., 2011). We found that knockdown of the basolateral determinants, Dlg1, Scrib and Lgl, resulted in the desired phenotype (Fig. 1F; Fig. S1; Movie 1). Given that the basolateral determinants often have similar mutant phenotypes (Bilder et al., 2000), we focused on Dlg1 for subsequent analyses. Knockdown of Dlg1 was confirmed by immunostaining with an anti-Dlg1 antibody (Fig. S2). In addition, *dlg1* RNAi embryos displayed defects in the localization of subapical landmarks, such as Bazooka (Baz; also known as Par-3), Canoe (Cno; also known as Afadin) and E-cadherin (Shg) (Fig. S3), consistent with a recent report (Bonello et al., 2019). Interestingly, we also detected subtle but consistent defects in F-actin localization in *dlg1* RNAi embryos (Fig. S4), which was not reported by Bonello et al. (2019). We noticed that a small fraction of the embryos showed more severe phenotypes, ranging from abnormal apical constriction to impaired cellularization (~22%, 8/37 embryos imaged). We focused our analysis on *dlg1* RNAi embryos that showed no visible defects during cellularization and apical constriction. This group of *dlg1* RNAi embryos exhibited a normal peak of V_x in the apical constriction phase and a reduced peak of V_x in the invagination phase (Fig. 1F,G). We confirmed that apical constriction in the *dlg1* RNAi embryos was normal by single-cell segmentation and tracking (Fig. 1H–J; $n=4$ embryos for each genotype; see Materials and Methods for details).

dlg1 RNAi embryos exhibit a delay in the transition between apical constriction and invagination

To further characterize the invagination phenotype in the *dlg1* RNAi embryos, we used multiphoton-based imaging to visualize the entire depth of the ventral furrow over the course of gastrulation (Fig. 2A; Movie 2). Consistent with our previous observations, in most *dlg1* RNAi embryos the apical constriction rate was similar to that of the control embryos (Fig. 2B; ventral cells achieved 70% apical area reduction in 8.3 ± 1.8 min in *dlg1* RNAi embryos, $n=8$ embryos, and 7.4 ± 1.5 min in control embryos, $n=4$ embryos; mean \pm s.d.). In control embryos, the constricting mesodermal cells formed a shallow furrow with a cup-shaped apical indentation at about 8–10 min after the onset of apical constriction. Immediately after this ‘transition’ point (T_{trans}), the tissue underwent rapid invagination until the furrow was fully internalized (Fig. 2A). In *dlg1* RNAi embryos, the apex of the shallow furrow remained close to the surface of the embryo for a longer period of time before it entered the rapid invagination phase (Fig. 2A; magenta box). To quantify this phenotype further, we measured the invagination depth, D , over time, which is defined as the distance between the apex of the furrow and the surface of the embryo (Fig. 2C). In *dlg1* RNAi embryos, it took a significantly longer time for the ventral furrow to reach $D=30$ μm compared with control embryos [Fig. 2D; 15.4 ± 3.4 min in *dlg1* RNAi (line 1) embryos, $n=20$ embryos, 17.1 ± 3 min in *dlg1* RNAi (line 2) embryos, $n=9$ embryos, and 12.6 ± 1 min in control

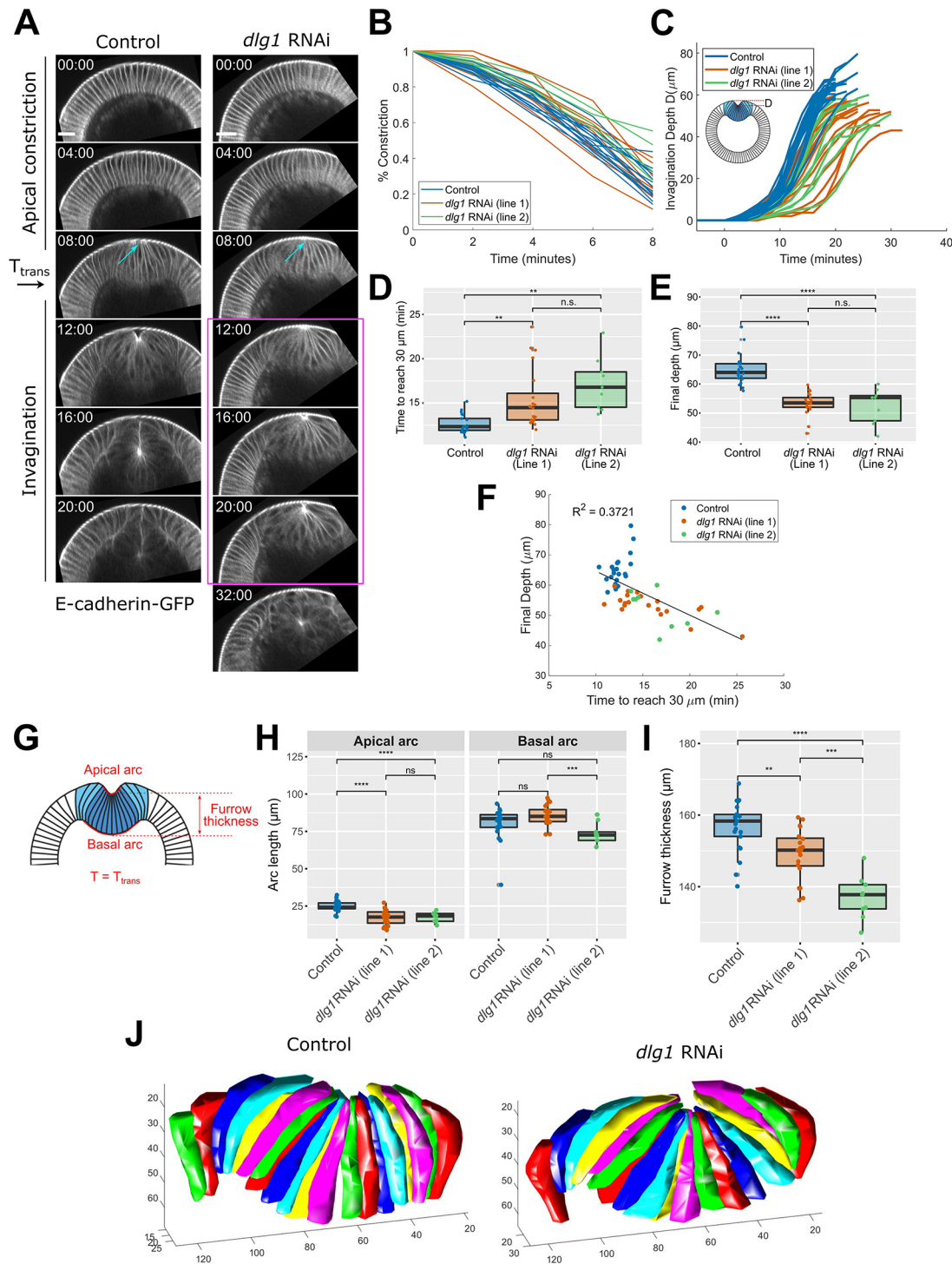


Fig. 2. *dlgl* RNAi embryos exhibit a delay in the transition between apical constriction and invagination, and invaginate less deeply. (A) Cross-section views of a control and *dlgl* RNAi mutant embryo during ventral furrow formation. Scale bars: 20 μm . Although apical constriction appears normal in the *dlgl* RNAi embryo (cyan arrows), there is a delay in the transition from apical constriction to invagination (magenta box). (B) Quantification of the normalized constriction cell domain width over time in control ($n=9$) and *dlgl* RNAi embryos ($n=11$). (C) Quantification of the invagination depth of the ventral furrow over time in control ($n=21$) and in two *dlgl* RNAi lines ($n=20$ and 9). (D) The time it takes for the ventral furrow to invaginate 30 μm , $T_{30\mu\text{m}}$, in the control and in the two *dlgl* RNAi lines shown in C. $**P \leq 0.01$ (unpaired, two-tailed Student's *t*-test). (E) Final invagination depth in the control and in the two *dlgl* RNAi lines shown in C. $****P \leq 0.0001$ (unpaired, two-tailed Student's *t*-test). (F) The final invagination depth and $T_{30\mu\text{m}}$ show an inverse correlation. (G) Schematic depicting the measurement of apical and basal arc lengths (outlined in red) and furrow thickness at T_{trans} (8 min). (H,I) Apical and basal arc length and furrow thickness comparisons for control ($n=21$) and two *dlgl* RNAi lines ($n=20$ and 9) at T_{trans} . $**P \leq 0.01$; $***P \leq 0.001$; $****P \leq 0.0001$ (unpaired, two-tailed Student's *t*-test). (J) 3D segmentation of the constricting cells and their non-constricting neighbors at T_{trans} . ns, not significant. For all box and whisker plots, the lower and upper hinges correspond to the first and third quartiles (the 25th and 75th percentiles), the horizontal line indicates the median, and the whiskers indicate the lowest and highest non-outlier values.

embryos, $n=21$ embryos; mean \pm s.d., same below]. In addition, the ventral furrow invaginated less deeply in the *dlg1* RNAi embryos, although the final morphology of the ventral furrow was largely normal [Fig. 2E; $53\pm4\ \mu\text{m}$ in *dlg1* RNAi (line 1) embryos, $n=20$ embryos, $52\pm6\ \mu\text{m}$ in *dlg1* RNAi (line 2) embryos, $n=9$ embryos, and $65\pm5\ \mu\text{m}$ in control embryos, $n=21$ embryos]. Interestingly, there was a moderate inverse correlation between the delay in invagination and the final invagination depth (Fig. 2F), suggesting that the two phenotypes are linked.

Next, we investigated whether the constricting, ventral mesodermal cells display any morphological defects prior to T_{trans} . First, we measured the size of the curved apical and basal surfaces ('arc length') of the intermediate furrow at T_{trans} (Fig. 2G). The apical arc length was on average 20% shorter in the *dlg1* RNAi embryos compared with the control embryos, whereas the basal arc length was similar between the two genotypes (Fig. 2H). Second, we estimated the apical-basal thickness of the intermediate furrow at T_{trans} by measuring the height of the mid constricting cells (Fig. 2G). The intermediate furrow in the *dlg1* RNAi embryos was on average 6% thinner than in the control embryos (Fig. 2I). Finally, 3D segmentation and reconstruction of the constricting cells at T_{trans} showed that, other than the mild reduction in apical-basal cell length, the morphology of the constricting cells and their spatial arrangement in the intermediate furrow were largely normal in the *dlg1* RNAi embryos (Fig. 2J). Together, these data indicate that ventral furrow formation in the *dlg1* RNAi embryos is relatively normal during the apical constriction phase.

It is worth noting that the expression of the invagination phenotype upon *Dlg1* knockdown is sensitive to the *GAL4* driver line that we used to drive the expression of *dlg1* shRNA. The driver line used in this work, which provides two copies of *GAL4*, one copy of *E-cadherin-GFP* and one copy of *Sqh-mCherry*, produced the most prominent invagination phenotype when combined with UAS *dlg1* shRNA (Materials and Methods). It is unclear whether this phenomenon is associated with the expression level of *dlg1* shRNA or the fluorescent markers specific to this driver. Nevertheless, the observed phenotype provided a useful starting point for us to further investigate the factors important for an effective transition between apical constriction and invagination.

The distribution of cortical myosin in the constricting cells is largely normal in the *dlg1* RNAi embryos during apical constriction

Next, we wondered whether other potential defects within the constricting cells could contribute to the invagination defects observed in the *dlg1* RNAi embryos. In particular, we examined whether knockdown of *Dlg1* affects apical, lateral or basal myosin in the constricting cells (Fig. 3A). We found that the constricting cells in the *dlg1* RNAi embryos underwent a similar basal myosin loss as in the control embryos (Fig. 3B, yellow arrowheads). In both the control and *dlg1* RNAi embryos, lateral *Sqh-mCherry* signal was sparse, but was similarly detectable in the constricting cells soon after the onset of gastrulation (Fig. 3C, red arrows). In accordance with the normal rate of apical constriction in the *dlg1* RNAi embryos, we found that apical myosin accumulation and distribution is similar between *dlg1* RNAi and control embryos (Fig. 3D,E; Movie 3). Furthermore, there were no obvious breaks within the supracellular myosin network in the *dlg1* RNAi embryos, suggesting that the network is properly interconnected (Movie 3). Together, these observations suggest that the invagination delay in the *dlg1* RNAi embryos is not caused by defects in the activation or spatial organization of myosin in the constricting cells.

Flanking, non-constricting cells in the *dlg1* RNAi embryos exhibit abnormal apical morphology during apical constriction

Because the constricting cells in the *dlg1* RNAi embryos behave relatively normally before the invagination phase, we investigated whether the delay in invagination is caused by defects in the non-constricting mesodermal cells adjacent to the constriction domain ('flanking cells'; Fig. 1A). Before gastrulation, the apical morphology of the flanking cells in the control and *dlg1* RNAi embryos is comparable. Differences between control and *dlg1* RNAi embryos first appeared during apical constriction. In control embryos, the apical domain of the flanking cells was moderately stretched along the medial-lateral axis by the neighboring constricting cells (Fig. 4A). In *dlg1* RNAi embryos, the apical domain of the flanking cells was stretched to a significantly greater extent than in the control embryos (Fig. 4A). Segmentation and quantification of the apical domains of the flanking cells at T_{trans} revealed that the apical domains of the flanking cells in the *dlg1* RNAi embryos are generally more elongated (Fig. 4B; Materials and Methods). The average area, average long axis and average aspect ratio of the apical domain in *dlg1* RNAi embryos were $74.1\pm27.2\ \mu\text{m}^2$, $14.4\pm4.0\ \mu\text{m}$, and 2.4 ± 0.8 , respectively, in comparison with $70.1\pm23.2\ \mu\text{m}^2$, $13.4\pm3.2\ \mu\text{m}$, and 2.1 ± 0.5 , respectively, in the control embryos (Fig. 4C; control: 883 cells in 14 embryos; *dlg1* RNAi: 1157 cells in 25 embryos).

Furthermore, we found that *dlg1* RNAi embryos with mild and severe invagination phenotypes exhibit differences in their flanking cell phenotype. On average, the flanking cells in the mild group (16/25 embryos) and the control group exhibited no significant difference in apical area and apical morphology (Fig. 4D-F). In contrast, the average aspect ratio and apical area of the flanking cells in the severe group was greater than in the control group (aspect ratio: 2.7 ± 0.2 compared with 2.1 ± 0.2 in control; apical area: $85.0\pm5.9\ \mu\text{m}^2$ compared with $71.2\pm9.4\ \mu\text{m}^2$ in control; control: $n=14$ embryos; severe *dlg1* group: $n=9$ embryos) (Fig. 4D-F). The correlation between the overstretched phenotype of the flanking cells and the delay in invagination in the *dlg1* RNAi embryos suggests a potential role for the flanking cells in facilitating the transition between apical constriction and invagination.

Aberrant apical myosin contractions in the flanking cells of *dlg1* RNAi embryos contribute to the hyper-stretched phenotype

Next, we sought to determine what causes the flanking cells in the *dlg1* RNAi embryos to become overstretched. It has been recently shown that, in addition to the constricting cells, the flanking cells in wild-type embryos also display apical myosin pulses during ventral furrow formation (Denk-Lobnig et al., 2021). In the constricting cells, the apical actomyosin network undergoes ratcheted contractions that result in a stepwise reduction of apical cell area. In contrast, the flanking cells accumulate lower levels of apical myosin, which result in unratcheted myosin pulses that do not lead to a net apical area reduction (Denk-Lobnig et al., 2021). We hypothesized that the unratcheted myosin pulses in the flanking cells allow the cells to temporarily resist the stretching induced by pulling forces from the constriction domain. We further hypothesized that this mechanism is no longer functional in the *dlg1* RNAi embryos, thereby leading to overstretching of the flanking cells.

To test these hypotheses, we first examined the relationship between myosin activity and apical cell dynamics in control flanking cells. Consistent with a previous report (Denk-Lobnig

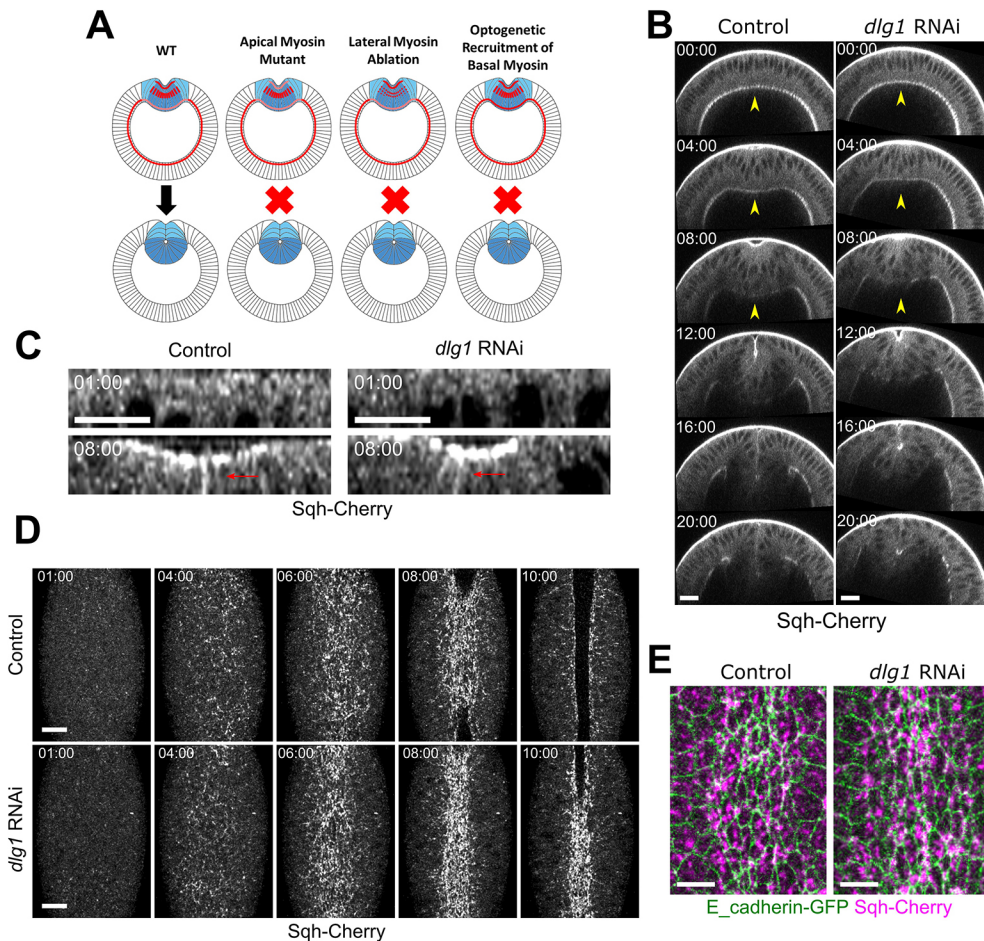


Fig. 3. Invagination defects in *dlg1* RNAi embryos are not likely due to abnormal myosin distribution or morphological defects in the constricting cells. (A) Schematic illustrating different scenarios in which defects in contractility can result in invagination defects. Mesodermal cells are marked in blue. Apical, lateral and basal myosin is indicated in red. (B) Projection of the cross-section view of a representative control and *dlg1* RNAi embryo expressing Sqh-mCherry and E-cadherin-GFP (not shown) imaged with a multiphoton microscope. Yellow arrowheads indicate basal myosin. Scale bars: 20 μ m. (C, D) Confocal images of a representative control and *dlg1* RNAi embryo expressing Sqh-mCherry and E-cadherin-GFP (not shown). Maximum projections of the cross-section view (C) and the en face view (D) are shown. Red arrows indicate lateral myosin. Scale bars: 20 μ m. (E) Confocal images of a representative control and *dlg1* RNAi embryo expressing Sqh-mCherry and E-cadherin-GFP during apical constriction. Scale bars: 10 μ m.

et al., 2021), we detected apical myosin coalescence in the flanking cells as apical constriction progressed (Fig. 5A; Movie 4). Compared with the constricting cells, accumulation of apical myosin in the flanking cells occurred later, and apical myosin intensity was much lower (Fig. S5A, cyan arrows). Typically, we were able to observe several rounds of myosin coalescence in an individual flanking cell before it disappeared from the surface of the embryo (Fig. S5B, red asterisks). Quantification of apical myosin intensity within individual flanking cells 4–10 min after the onset of apical constriction (Materials and Methods) revealed repeated rise and fall of myosin intensity in the flanking cells, with a general trend of intensity increase over time (Fig. 5B). To analyze the impact of myosin coalescence on apical cell shape change, we identified individual myosin pulses and examined how apical cell area changes during a 96-s interval centered around the pulse peak time (Fig. 5C,D, time 00:00; Materials and Methods). During a pulse, apical myosin generally reached its highest intensity at the pulse peak time (Fig. 5G). We found that myosin pulses in control flanking cells were often, albeit not always, accompanied by a reduction in cell area (Fig. 5C,E; Fig. S6A). To assess the functional relevance of this phenomenon, we compared apical cell area change during myosin pulses and during 96-s intervals between two successive myosin pulses ('off-pulses'). As expected, apical myosin intensity at the pulse peak time was significantly higher during pulses than during off-pulses (Fig. 5H). Interestingly, we found that during pulses the average apical area of the flanking cells barely changed. In contrast, apical cell area increased significantly during off-pulses (Fig. 5I,J; apical area change was $-0.4 \pm 11.8 \mu\text{m}^2$ for

pulses and $7.1 \pm 12.1 \mu\text{m}^2$ for off-pulses; $n=56$ pulses and 41 off-pulses, $P=0.0018$). The change in length of the apical domain along the medial-apical axis ('apical length') displayed a similar trend as the change in apical cell area (Fig. 5K,L; apical length change was $1.1 \pm 2.3 \mu\text{m}$ for pulses and $2.0 \pm 2.3 \mu\text{m}$ for off-pulses; $P=0.036$). A similar trend was observed when we normalized apical area and apical length by their initial size (Fig. S6B). Together, these results support a model in which myosin pulses in the flanking cells function to restrain stretching of the apical domain, presumably by counteracting pulling forces from the constriction domain.

Next, we extended the analysis to the *dlg1* RNAi embryos. Like in the control flanking cells, the mutant flanking cells also displayed cycles of myosin pulses that had similar frequency and average peak myosin intensity (Fig. 5B,G,H; Fig. S6C). However, myosin pulses in the flanking cells of *dlg1* RNAi embryos were rarely associated with either reduction or stabilization of apical cell area or apical length (Fig. 5D,F; Fig. S6A). The average increase in apical cell area and apical length during pulses in the mutant flanking cells was significantly higher than in the control flanking cells and appeared to be more similar to non-pulses (Fig. 5I–L; apical area change was $8.5 \pm 13.2 \mu\text{m}^2$ for *dlg1* pulses and $12.6 \pm 12.0 \mu\text{m}^2$ for *dlg1* off-pulses; $n=143$ pulses and 100 off-pulses; $P=5.6 \times 10^{-6}$ for comparison between control and *dlg1* pulses; apical length change was $3.1 \pm 2.4 \mu\text{m}$ for *dlg1* pulses and $3.5 \pm 2.3 \mu\text{m}$ for *dlg1* off-pulses; $P=1.4 \times 10^{-7}$ for comparison between control and *dlg1* pulses). These observations suggest that myosin pulses in the mutant flanking cells are much less effective at restraining apical cell stretching than those in control flanking cells. Further analysis revealed that the coupling

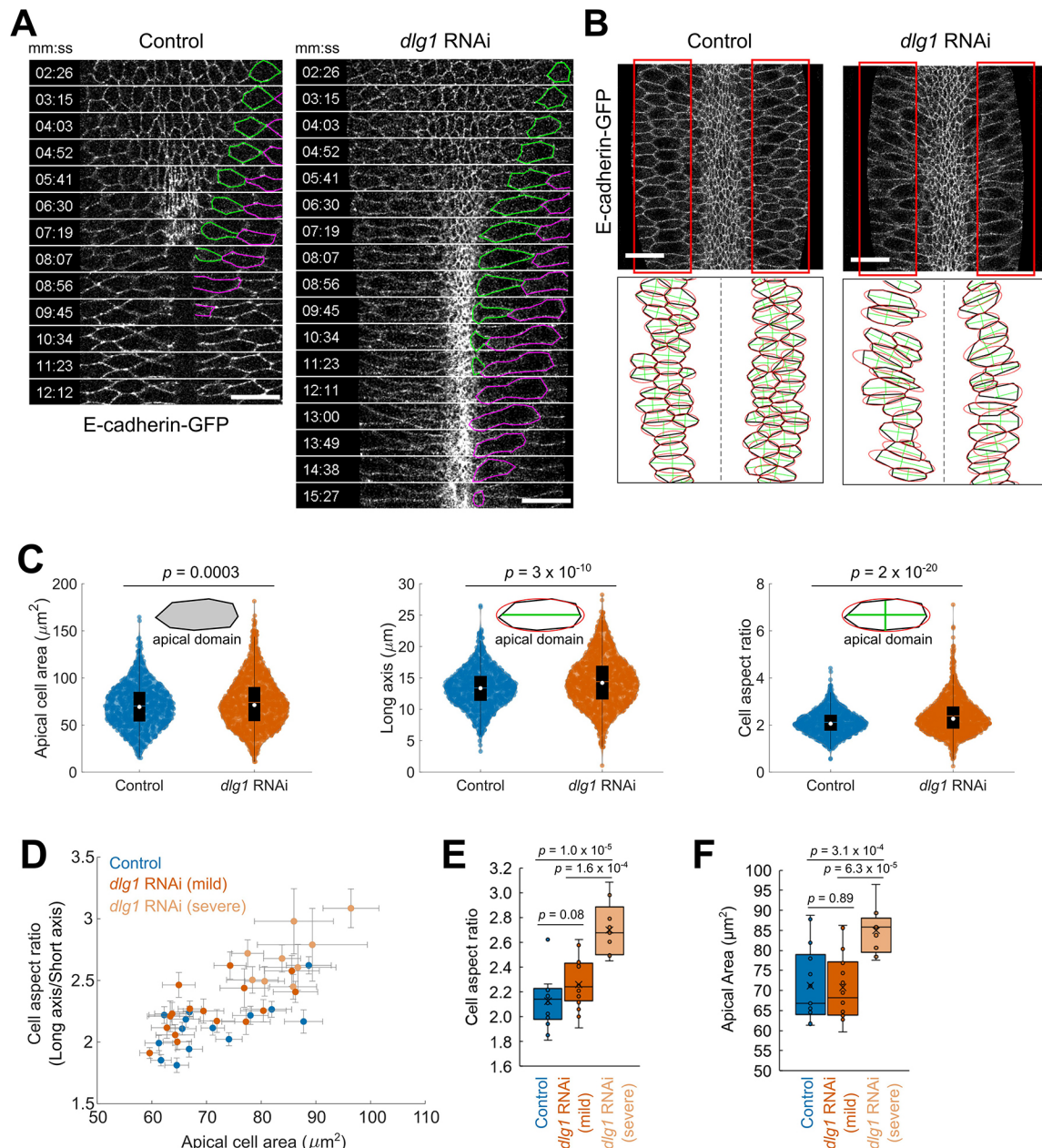


Fig. 4. Flanking non-constricting cells in *dlg1* RNAi embryos are overstretched during apical constriction. (A) Time-lapse images of a control embryo and a *dlg1* RNAi embryo during ventral furrow formation. Ventral surface views are shown. Scale bars: 20 μ m. (B) Top: Surface view of a control embryo and a *dlg1* RNAi embryo at T_{trans} . Bottom: The apical cell shape of the flanking non-constricting cells [the area in the red boxes in A at T_{trans} was segmented (black) and fitted to an ellipse (red)]. The long and short axes are shown in green. (C) Measurement of geometrical properties of the apical domain of the flanking cells at T_{trans} . Control: $n=883$ cells from 14 embryos. *dlg1* RNAi: $n=1157$ cells from 25 embryos. Schematics illustrate the measurements taken. For all violin plots, the lower and upper limits of the black box correspond to the first and third quartiles (the 25th and 75th percentiles), the horizontal line indicates the mean, and the white point in the black box indicates the median. (D) The aspect ratio of the flanking non-constricting cells plotted against apical area. Each circle shows the average measurement ($n=52 \pm 18$, mean \pm s.d., cells per embryo). Error bars represent s.e.m. Control: $n=14$ embryos; mild *dlg1* RNAi: $n=16$ embryos; severe *dlg1* RNAi: $n=9$ embryos. (E,F) Distribution of the apical cell aspect ratio (E) and apical cell area (F) in control, *dlg1* RNAi (mild) and *dlg1* RNAi (severe) embryos. Unpaired, two-tailed Student's *t*-test was used for statistical analyses. For all box and whisker plots, the lower and upper hinges correspond to the first and third quartiles (the 25th and 75th percentiles), the horizontal line indicates the median, and the whiskers indicate the lowest and highest non-outlier values.

between myosin pulses and local cell shape deformation is reduced in the mutant flanking cells (Fig. 5M-Q; Materials and Methods). Together, our results suggest that reduced coupling between contractile myosin and cell-cell boundaries in the mutant flanking cells impairs their ability to resist cell stretching.

Interestingly, we noticed that the adherens junction marker E-cadherin-GFP shows reduced intensity at the subapical region in the

mutant flanking cells (Fig. S7). In the constricting mesodermal cells, the apical myosin network exerts contractile forces at cell-cell boundaries by anchoring at the apical adherens junctions (Martin et al., 2010). The observed defect in apical adherens junctions in the mutant flanking cells led us to hypothesize that the 'unclutched' myosin pulses are the result of impaired actomyosin fiber attachments at the cell-cell junctions. Consistent with this

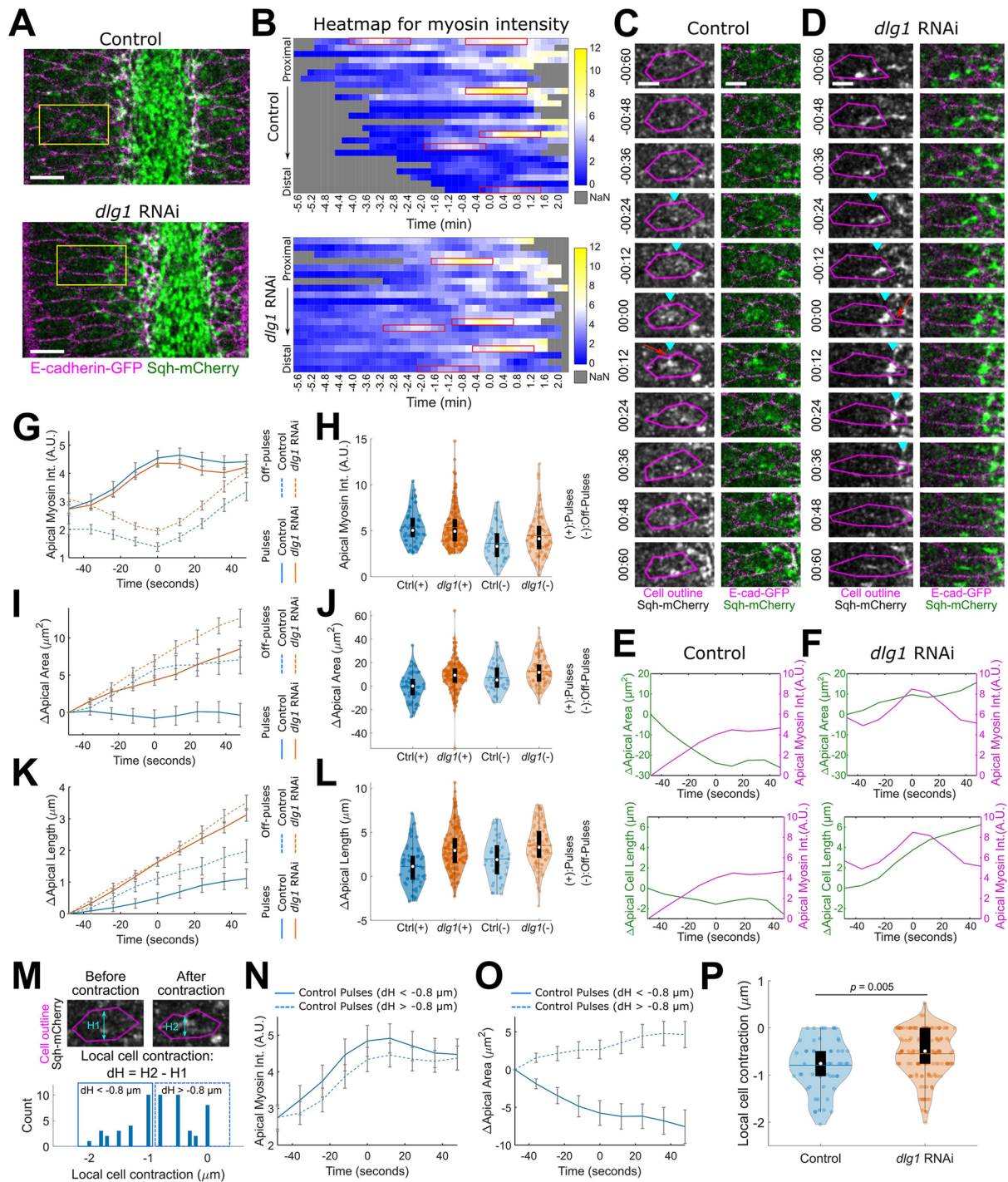


Fig. 5. Knockdown of Dlg1 affects apical myosin contractions in the flanking cells. (A) Ventral surface view of a control embryo and a *dlg1* RNAi embryo expressing E-cadherin-GFP and Sqh-mCherry at the end of the apical constriction phase. The flanking cells highlighted by yellow boxes are presented in C and D. Scale bars: 10 μm . (B) Heatmap showing apical myosin intensities over time in individual flanking cells. Each row corresponds to one cell. The flanking cells are ordered based on their proximity to the ventral midline. T=0:00 (mm:ss) corresponds to T_{trans} . Gray indicates data unavailable (NaN, Not a Number). (C,D) Examples of apical myosin coalescence observed in the flanking cells in control and *dlg1* RNAi embryos. T=0:00 (mm:ss) corresponds to the pulse peak. Both cells are on the left of the ventral midline. Myosin coalescence is indicated by cyan arrowheads. Local cell contractions are indicated by red arrows. Scale bars: 10 μm . (E,F) Apical myosin intensity and changes in apical cell area and apical cell length over time in cells shown in C and D, respectively. Time zero is the pulse peak. (G,I,K) Average trend of apical myosin intensity, apical area change, and apical length change over time for pulses and off-pulses in the flanking cells; 56 pulses and 41 off-pulses from four control embryos and 143 pulses and 100 off-pulses from eight *dlg1* RNAi embryos were analyzed. Error bars represent s.d. (H) Distribution of apical myosin intensity at the pulse peak. (J,L) Distribution of apical area change and apical length change. (M) Top: Schematic showing measurement of local cell contraction (dH) during a pulse in the flanking cells. Bottom: Distribution of dH for pulses in control embryos. (N,O) Average trend of apical myosin intensity and apical area change over time for control pulses associated with high ($dH < -0.8 \mu\text{m}$) or low ($dH > -0.8 \mu\text{m}$) levels of local cell contraction. Error bars represent s.d. (P) Distribution of dH for pulses in control and *dlg1* RNAi embryos. For all violin plots, the lower and upper limits of the black box correspond to the first and third quartiles (the 25th and 75th percentiles), the horizontal line indicates the mean, and the white point in the black box indicates the median.

hypothesis, we frequently observed rapid flow of myosin to the leading edge (the edge closer to the midline) of the flanking cells in the *dlg1* RNAi embryos, an expected phenomenon when anchoring of actomyosin at cell-cell boundaries is impaired (Fig. 5D, cyan arrowheads).

It is worth noting that the extent of apical area increase in the flanking cells during off-pulses was greater in the *dlg1* RNAi embryos than in the control embryos (Fig. 5I,K), suggesting that, in addition to unclutched myosin pulses, other factors may also contribute to the overstretched phenotype. By applying pulling forces using magnetic tweezers on a group of ventrolaterally localized cells before gastrulation (Materials and Methods), we found that knockdown of Dlg1 alters the mechanical properties of these cells, making them more prone to irreversible deformation (Fig. S8). Although we were not able to specifically target the flanking cells, this result raises an interesting possibility that changes in tissue mechanical properties upon Dlg1 knockdown could also contribute to the overstretched phenotype of the flanking cells.

Hyper-stretching of the flanking cells in the *dlg1* RNAi embryos slows down the ventral movement of the ectodermal tissue during ventral furrow formation

During ventral furrow formation, the neighboring ectodermal tissue moves towards the ventral midline as the mesoderm internalizes. We predicted that hyper-stretching of the flanking cells in the *dlg1* RNAi embryos would delay ventral movement of the ectodermal tissue (Fig. 6A). Because overstretching of the flanking cells mainly occurs at the apical domain (Fig. 6H), we examined surface projections of the embryos from the multiphoton movies described in Fig. 2. For each embryo, we segmented the apical cell outlines of a single row of cells along the medial-lateral axis and tracked them over time (Fig. 6B). We found that the movement of the ectodermal cells towards the ventral midline was substantially slower in the *dlg1* RNAi embryos (Fig. 6C,D). In theory, both overstretching of the flanking cells and delayed mesoderm invagination could result in a reduced rate of ectodermal movement. We therefore examined whether this defect could be detected prior to T_{trans} , before invagination of the mesoderm occurs. As illustrated in Fig. 6E, we predicted that prior to T_{trans} , hyper-stretching of the flanking cells in the *dlg1* RNAi embryos would mostly affect the rate of ectodermal cell movement and, to a lesser extent, flanking cell movement. Our measured velocities of cell movement during the first 8 min of ventral furrow formation closely matched the predicted outcome (Fig. 6F). Notably, there was a moderate correlation between the rate of ectodermal cell movement during apical constriction and the delay in invagination (Fig. 6G). This result led us to hypothesize that proper coupling between the constricting cells and the ectodermal tissue is important for a robust transition between apical constriction and invagination.

Disruption of the flanking cells by laser ablation or optogenetic-mediated disassembly of F-actin delays the transition between apical constriction and invagination

The phenotypic analysis of *dlg1* RNAi embryos prompted us to investigate whether disrupting the flanking cells is sufficient to cause invagination defects. In our first approach, we used a focused beam of a near-infrared laser to disrupt the flanking cells in wild-type embryos during apical constriction. To avoid any adverse effects from wound healing responses, we carefully tuned the laser power such that no visible damage on the plasma membrane was

observed after laser ablation (Materials and Methods). To disrupt the flanking cells, we scanned a focused laser beam across a $\sim 170 \mu\text{m} \times 10 \mu\text{m}$ region at the apical surface spanning one or two columns of flanking cells on both sides of the constriction domain (Fig. 7A,B). We started laser ablation approximately 2–3 min before T_{trans} and repeated ablation every 68 s to achieve prolonged disruption (see Materials and Methods for rationale). After laser ablation, the ablated region immediately expanded, and the non-constricting tissue adjacent to the treated region underwent immediate retraction (Fig. 7C, cyan arrows; Movie 5). This observation confirms that the flanking cells are under tension during apical constriction. After the initial retraction, the subsequent movement of the ectodermal cells towards the ventral midline was also interrupted (Fig. 7C, cyan arrows; Movie 5). We did not observe any obvious impacts on the constriction domain after laser ablation; no relaxation happened, and the cells continued to constrict apically (Fig. 7C, magenta arrows; Movie 5). Most interestingly, this interruption was associated with a delay in the transition between apical constriction and invagination (Fig. 7D–F; Movie 5), similar to what we observed in the *dlg1* RNAi embryos. These results demonstrate that disruption of the flanking cells is sufficient to cause a delay in invagination.

In the second approach, we utilized a previously published Cryptochrome 2 (CRY2)-CIBN optogenetic tool to downregulate actin in the flanking cells during apical constriction (Guglielmi et al., 2015). We anticipated that apical actomyosin contractions and resistance in the flanking cells would be disrupted after targeted stimulation at the apical region. In this optogenetic system, CIBN is anchored to the plasma membrane (CIBN-pm). Upon light stimulation, CIBN recruits cytoplasmic CRY2-OCRL (tagged with mCherry) to the plasma membrane (Fig. 8A,B). OCRL is the catalytic domain of the inositol polyphosphate 5-phosphatase (Zhang et al., 1995). Once at the plasma membrane, OCRL converts $\text{PI}(4,5)\text{P}_2$ into $\text{PI}(4)\text{P}$, which results in disassembly of cortical actin (Guglielmi et al., 2015; Fig. S9). We found that ventral furrow formation proceeds normally in most embryos expressing the optogenetic constructs when they were imaged with the 1040 nm laser, which does not stimulate CRY2-OCRL (Guglielmi et al., 2015). A small percentage of embryos (3/18 embryos examined) were morphologically abnormal during apical constriction and failed to invaginate. Embryos in both the control and stimulated groups that showed defects in apical constriction were not included in our analysis. We then tested whether stimulation of the flanking cells during apical constriction would affect furrow invagination. For technical reasons (see Materials and Methods for details), we chose to stimulate a $170 \mu\text{m} \times \sim 30 \mu\text{m}$ rectangular region that spanned four to five columns of non-constricting cells (approximately three columns of flanking cells and one or two columns of adjacent ectodermal cells) next to the constriction domain (Fig. 8A,B). Stimulating this region during apical constriction consistently resulted in a delay in furrow invagination (Fig. 8C–E; Movie 6). The apical domain of the stimulated cells became more elongated and adopted a more irregular shape than cells in wild-type embryos (Fig. 8F). This behavior is reminiscent of the flanking cells in the *dlg1* RNAi embryos. Taken together, the laser ablation and optogenetic experiments in the wild-type embryos provide additional evidence that maintaining the mechanical integrity of the flanking cells, and thereby the coupling between the constriction domain and the ectodermal tissue, is important for an efficient transition between apical constriction and invagination.

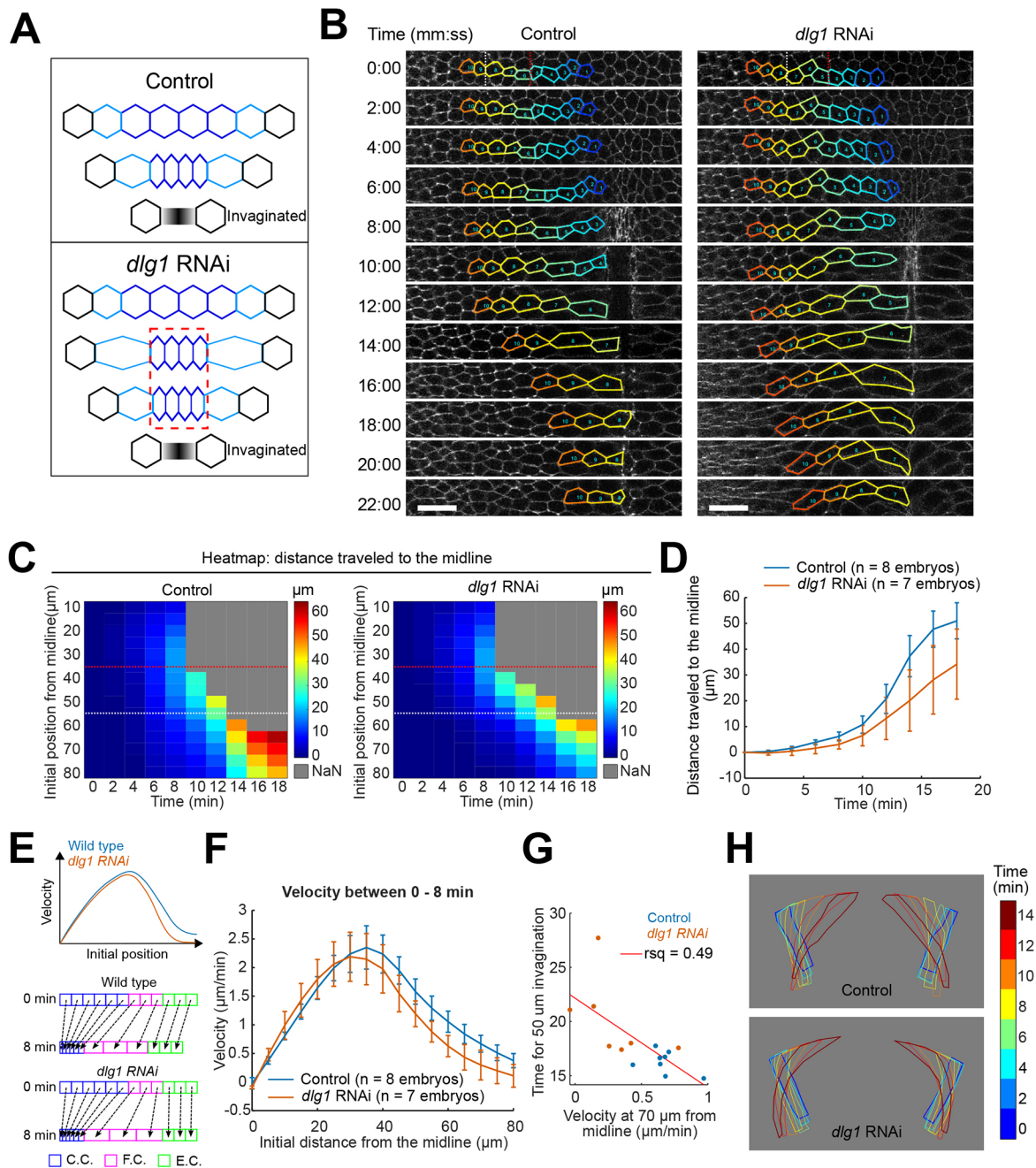


Fig. 6. Ventrally directed movement of the lateral ectodermal cells is delayed in *dlg1* RNAi embryos. (A) Schematic illustrating the shape change of the apical domain of the constricting cells (dark blue), the flanking cells (light blue) and the ectodermal cells (black) during apical constriction. The dashed red box highlights the invagination delay in the *dlg1* RNAi embryos. (B) Movie stills showing the apical surface of cells (outlined) initially located at different locations along the medial-lateral axis on the left side of the ventral midline. The red and white dotted lines indicate the boundary between the constricting and the flanking cells, and the boundary between the flanking cells and the ectodermal cells, respectively (same for C). Scale bars: 20 μ m. (C) Heatmaps for two example embryos showing the distance that cells initially located at different medial-lateral positions traveled towards the ventral midline over time. Error bars represent s.d. (D) Distance traveled towards the midline for ectodermal cells initially located 70 μ m away from the midline. Error bars represent s.d. (E) Schematic showing cell velocity during apical constriction as a function of the initial medial-lateral position of the cells. C.C., constricting cells; E.C., ectodermal cells; F.C., flanking cells. (F) Measurement of cell velocity during apical constriction as a function of the initial medial-lateral position of the cells. Error bars represent s.d. (G) A reduced rate of ectodermal cell movement during apical constriction correlates with invagination delays. (H) Cross-section views of a 2D outline of two flanking cells over time in representative control and *dlg1* RNAi embryos.

DISCUSSION

Apical constriction is an important mechanism that promotes folding of flat epithelia in a variety of tissue morphogenetic processes. However, how apical constriction results in tissue folding is not fully understood. In this work, we present evidence that

during *Drosophila* ventral furrow formation the integrity of the flanking cells adjacent to the constriction domain is important for a robust transition between apical constriction and invagination. We found that knockdown of the basolateral determinant Dlg1 does not affect apical myosin activation or apical constriction, but still results

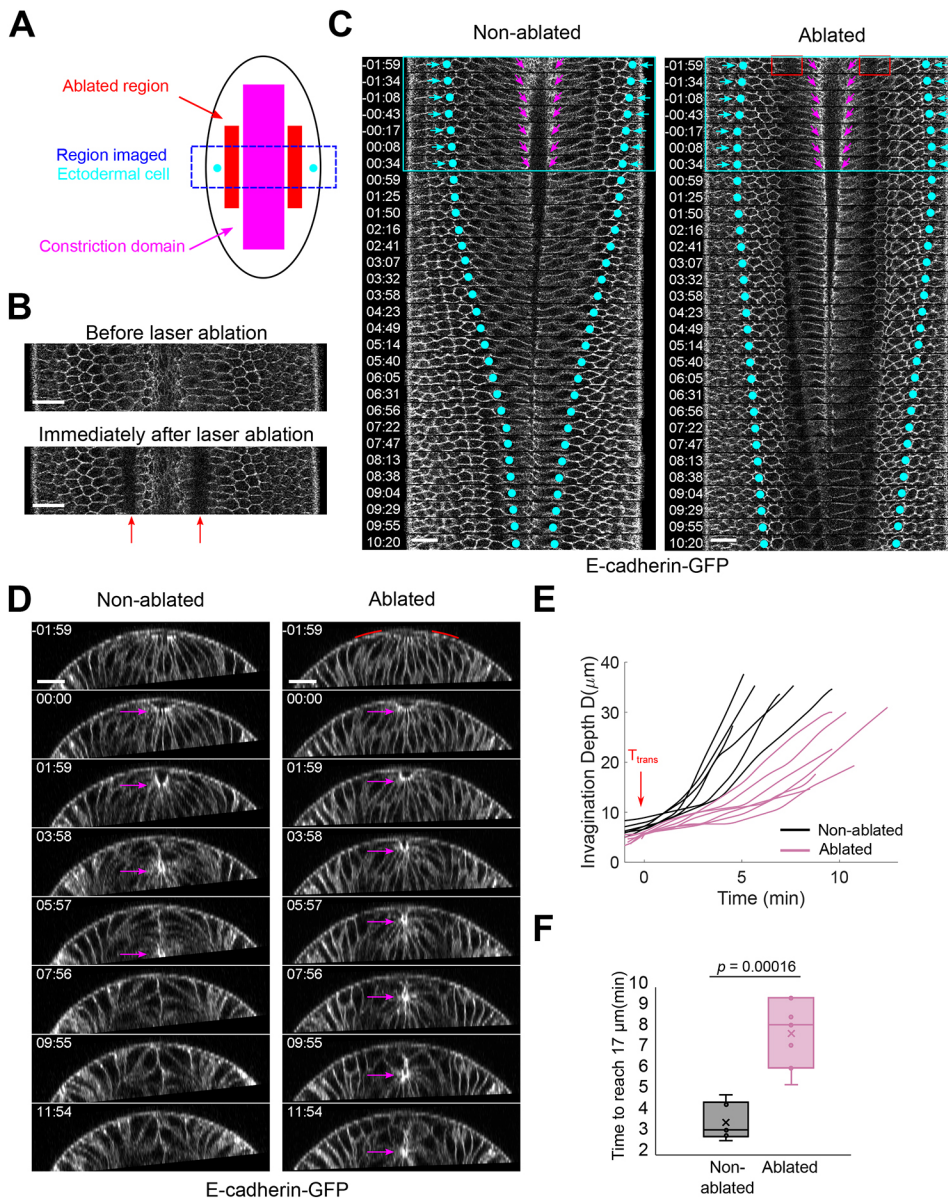


Fig. 7. Laser ablation of flanking non-constricting cells during apical constriction in wild-type embryos delays the transition between apical constriction and invagination. (A) Schematic illustrating the experimental design for laser ablation of the flanking cells in a *Drosophila* embryo. (B) Ventral surface view of an embryo before (top) and after (bottom) laser ablation. Red arrows indicate the ablated regions. Scale bars: 20 μm . (C, D) Representative en face (C) and cross-section (D) images of stage-matched wild-type embryos undergoing ventral furrow formation with or without laser ablation (red boxes in C; red lines in D). $T=00:00$ (mm:ss) corresponds to T_{trans} . Cyan circles in C indicate the position of two ectodermal cells that temporarily underwent retraction following laser ablation (cyan boxes and arrows). The constriction domain is not affected (magenta arrows in C). Magenta arrows in D indicate the apex of the ventral most cells. Scale bars: 20 μm . (E) Invagination depth, D , over time in non-ablated ($n=6$) and ablated ($n=7$) embryos. (F) Time taken for the ventral furrow to reach $D=17 \mu\text{m}$ in non-ablated and ablated embryos. Unpaired, two-tailed Student's t -test was used for statistical analysis. The lower and upper hinges correspond to the first and third quartiles (the 25th and 75th percentiles), the horizontal line indicates the median, and the whiskers indicate the lowest and highest non-outlier values.

in a delay in invagination. In contrast to the minor defects we observed in the constriction domain of the *dlg1* RNAi embryos, the apical domain of the flanking cells becomes substantially overstretched as the ventral mesodermal cells constrict. The severity of this phenotype correlates with the extent of delay in invagination. Using two separate approaches, we directly tested the role of the flanking cells in wild-type embryos during ventral furrow formation. Both manipulations resulted in a delay in invagination, without perturbing apical constriction, much like in the *dlg1* RNAi embryos. Although we could not directly test the causal relationship between the flanking cell phenotype and the delay in invagination in the *dlg1* RNAi embryos, the invagination defects observed upon disruption of the flanking cells in the wild-type embryos provide direct evidence for their function in tissue folding.

The mechanism by which the flanking cells contribute to invagination remains unclear. We found that defects in the flanking cells in *dlg1* RNAi embryos result in a delay in ventrally directed movement of the ectodermal cells during apical constriction and invagination. A similar delay in ectodermal movement was also

observed when we ablated the flanking cells. These results suggest that the flanking cells are important for coupling the movement of the constricting cells and the surrounding ectodermal tissue. Given that similar invagination phenotypes were observed in all three scenarios where the flanking cells were impaired, we propose that tissue-level coupling between the mesoderm and the ectoderm is important for promoting mesoderm invagination (Fig. 9). How this coordination promotes tissue folding remains to be elucidated. Interestingly, it has been previously shown that ventral movement of the ectoderm is not merely a consequence of mesoderm invagination. It can still occur, albeit with a reduced speed, in mutants in which apical constriction is completely abolished (Rauzi et al., 2015). Therefore, it is attractive to propose that ectodermal movement plays an active role in promoting the transition between apical constriction and invagination, perhaps by providing pushing forces on both sides of the ventral furrow. In such a scenario, appropriate coupling between the mesoderm and the ectoderm may facilitate mesoderm invagination by enabling transmission of forces from the ectoderm to the mesoderm. Future investigation will be necessary to test these hypotheses.

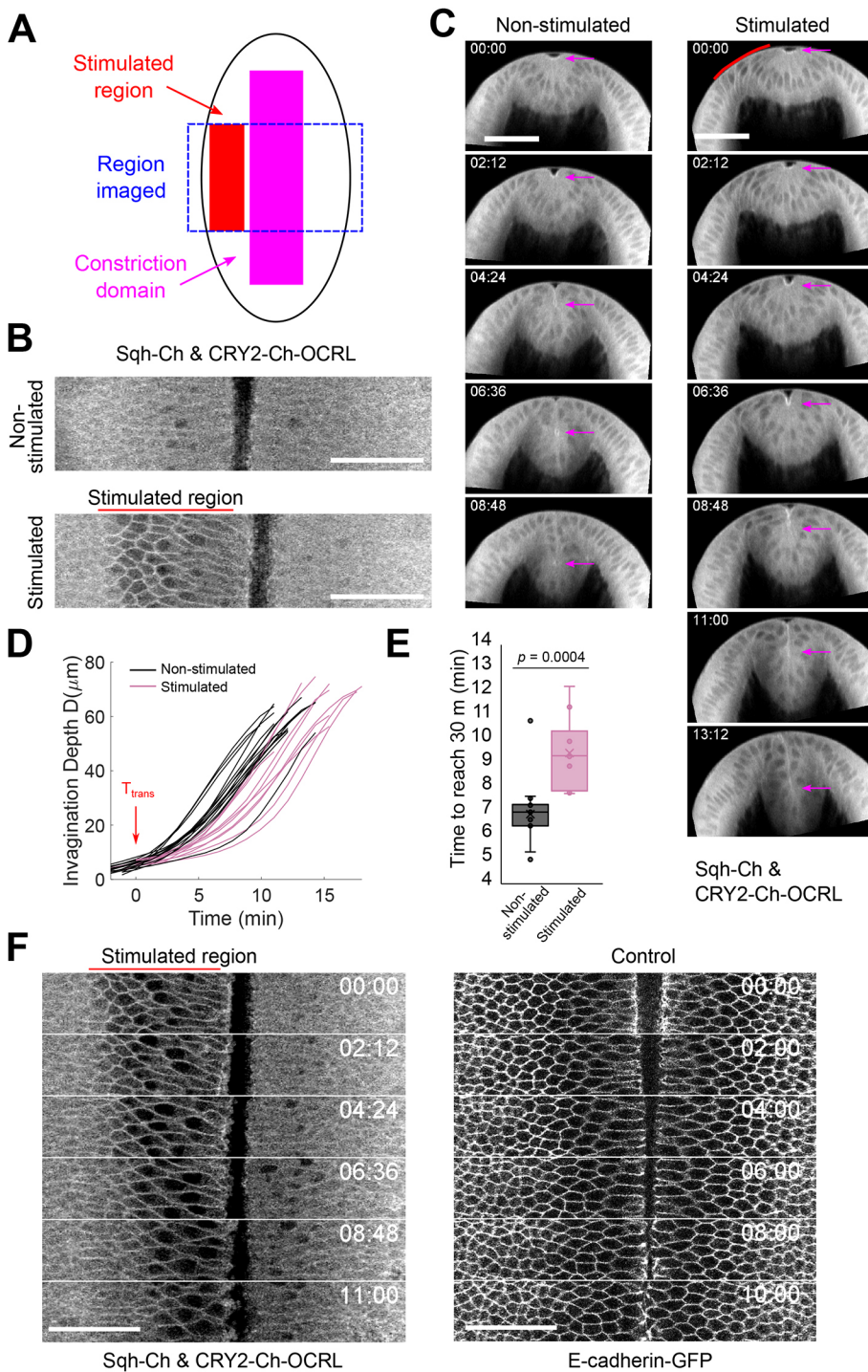


Fig. 8. Downregulation of cortical F-actin in the lateral non-constricting cells delays the transition between apical constriction and invagination. (A) Schematic illustrating the optogenetic experimental design in a *Drosophila* embryo. (B,C) Representative surface view (B) and cross-section (C) images of stage-matched embryos expressing CIBN-pm-GFP and CRY2-mCherry-OCRL undergoing ventral furrow formation in the presence or absence of stimulation. T=0:00 (mm:ss) corresponds to T_{trans} . The red lines highlight the stimulated region. Magenta arrows in C indicate the apex of the ventral-most cells. Scale bars: 50 μ m. (D) Invagination depth, D, over time in the absence ($n=15$ embryos) or presence ($n=10$ embryos) of stimulation. (E) Time taken for the ventral furrow to reach D=30 μ m in non-stimulated and stimulated embryos. Unpaired, two-tailed Student's *t*-test was used for statistical analysis. The lower and upper hinges correspond to the first and third quartiles (the 25th and 75th percentiles), the horizontal line indicates the median, and the whiskers indicate the lowest and highest non-outlier values. (F) Movie stills showing the surface view of a representative stimulated embryo expressing CIBN-pm-GFP and CRY2-mCherry-OCRL (left). The surface view of a representative control embryo expressing E-cadherin-GFP, but not the optogenetic constructs is shown for comparison (right).

Although the mechanism by which Dlg1 regulates the properties of the flanking cells is not fully understood, our data suggest that the overstretched phenotype of the flanking cells is partially due to aberrant coupling of apical myosin contractions to the cell junctions. Weakening adherens junctions or disrupting the link between adherens junctions and the actomyosin network has been associated with ineffective myosin-driven cell contractions (Roh-Johnson et al., 2012; Sawyer et al., 2009). We postulate that in wild-type flanking cells, the actomyosin fibers are strongly connected to the cell-cell junctions. This allows the apical myosin network to contract in a clutched/engaged manner, generate contractile forces

on the cell-cell boundary, and help resist pulling forces from the constriction domain. In the flanking cells of the *dlg1* RNAi embryos, attachment between the actomyosin network and the cell-cell junctions is impaired. In this case, the unclutched/disengaged actomyosin contractions are not sufficient to resist pulling forces from the constriction domain, and the flanking cells become hyper-stretched (Fig. 9A).

Past studies of apical constriction-mediated epithelial folding have mostly focused on the role of active forces generated in the constricting cells. The potential contribution of cells outside of the constriction domain has not been well studied. Our work indicates

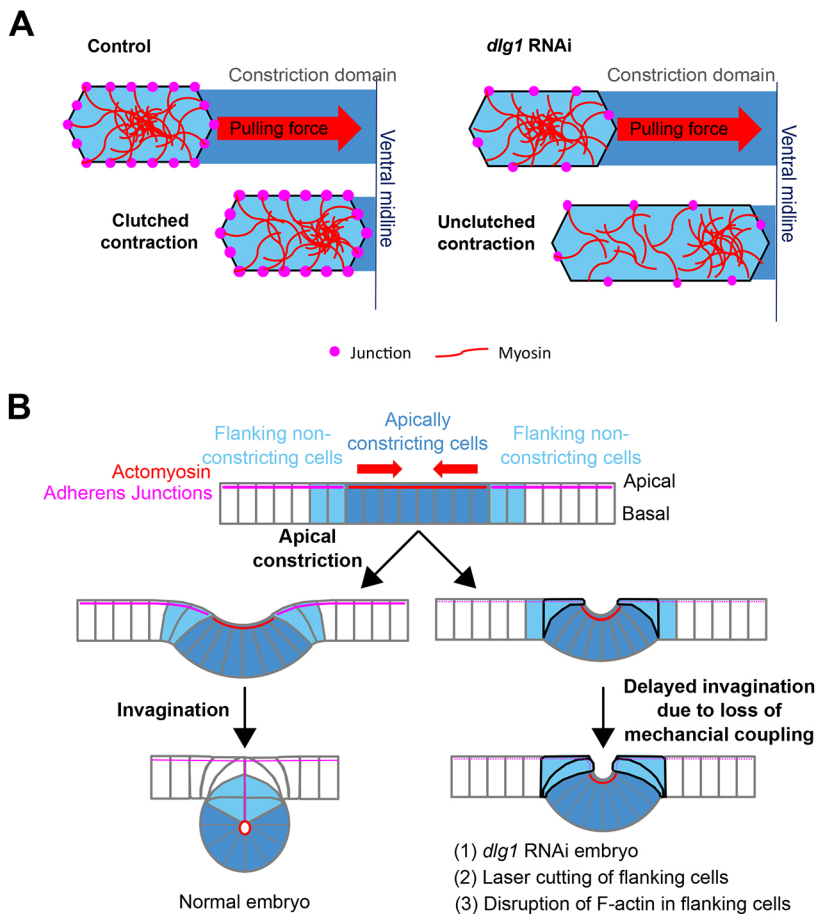


Fig. 9. A working model for cellular mechanics and tissue coordination during epithelial folding. (A) In control embryos, effective force transmission between the actomyosin network (red) and the adherens junctions (pink) allows the flanking cells to undergo clutched contractions, which enable the flanking cells to resist pulling from the constricting cells. In *dlg1* RNAi embryos, myosin contractions become 'unclutched' in the flanking cells. As a result, the mutant flanking cells are unable to resist pulling from the constricting cells and become hyper-stretched. (B) In control embryos, the flanking non-constricting cells (light blue) mediate mechanical coordination between the constriction domain (dark blue) and the non-constricting ectodermal tissue (white). This tissue-level coordination is important for an effective transition from apical constriction to invagination. When the mechanical integrity of the flanking cells is disrupted, the flanking cells become overstretched (black cell outlines), which impairs the mechanical coordination between the constricting cells and the surrounding ectodermal tissue, and results in a delay in invagination.

that the integrity of the flanking cells adjacent to the constriction domain can influence invagination by mediating coupling between the constricting cells and the ectodermal tissue. Furthermore, we demonstrate that this coupling requires the ability of the flanking cells to resist stretching from the constriction domain, which is dependent on clutched apical myosin contractions. In the future, it will be important to elucidate the actual mechanical contributions of non-constricting tissues during tissue folding and to further investigate how *Dlg1* regulates mechanical properties at the cell and tissue level.

MATERIALS AND METHODS

Fly stocks and genetics

E-cadherin-GFP (ubi-DE-cad-GFP) was described by Morin et al. (2001), Sqh-GFP by Royou et al. (2002) and Sqh-mCherry by Martin et al. (2009). Utr-Venus was a gift from the lab of A. Sokac (University of Illinois at Urbana-Champaign, IL, USA). UAS-Baz-GFP was a gift from the lab of Y. C. Wang (RIKEN, Japan). The following CPTI (Cambridge Protein Trap Insertion) stock was obtained from the Kyoto *Drosophila* Stock Center: Cno-YFP (115111). The following lines were obtained from the Bloomington *Drosophila* Stock Center: *dlg1* TRiP (36771, 33620), *dlg1*[2]/FM7a (36278), *dlg1*[5]/FM7a (36280), *scrib* TRiP (39073, 38199, 58085), and *lgl* TRiP (35773, 38989). The TRiP lines were crossed to a maternal GAL4 driver line, Maternal-Tubulin-Gal4 67.15 ('Mat67; Mat15'; Hunter and Wieschaus, 2000), for expression of shRNA during oogenesis. The following optogenetic lines were a gift from the De Renzis lab (EMBL, Heidelberg, Germany): (1) w[*]; UASp-CIBN-pmGFP/CyO; Sb/TM3, (2) UASp-pmCIBN/FM6; Sb/TM6B, and (3) UASp-CRY2-OCRL/TM3.

To examine gastrulation defects in embryos with maternal knockdown of specific candidate genes via RNA interference ('RNAi embryos'), female

flies from specific TRiP lines were crossed to Mat67 Sqh-mCherry; Mat15 E-cad-GFP/TM3 males to generate Mat67 Sqh-mCherry/TRiP; Mat15 E-cad-GFP/+ or Mat67 Sqh-mCherry/+; Mat15 E-cad-GFP/TRiP flies. The embryos derived from these flies were used for morphological analysis and analysis of adherens junction organization. To generate controls for the knockdown experiments, *y w f* females were crossed to Mat67 Sqh-mCherry; Mat15 E-cad-GFP/TM3 males to generate Mat67 Sqh-mCherry/+; Mat15 E-cad-GFP/+ flies. The embryos derived from these flies were used as control.

Similar crosses were made to examine the localization of specific proteins in RNAi embryos (F-actin, Cno and Baz). The maternal GAL4 lines used for these studies were: (1) Mat67 Sqh-mCherry; Mat15 Utr-Venus/TM3, (2) Mat67 Sqh-mCherry; Mat15 Cno-YFP/TM3, and (3) Mat67 Baz-GFP/CyO; Mat15 Sqh-mCherry. In addition, embryos derived from Mat67 Sqh-mCherry/+; Mat15 Utr-Venus/*dlg1* TRiP flies were used for the magnetic tweezer experiments. Embryos derived from wild-type flies containing ubi-E-cadherin-GFP were used for laser-ablation experiments.

To examine the actin phenotype in *dlg1* maternal mutant embryos, females from the *dlg1*⁵/FM7a; Utr-Venus Sqh-mCherry/TM3 stocks were crossed to *dlg1*²/Y males to generate *dlg1*²/*dlg1*⁵; Utr-Venus Sqh-mCherry/+ transheterozygous mutant flies. Embryos derived from these flies were imaged as *dlg1* maternal mutant embryos. *dlg1*²/FM7a; Utr-Venus Sqh-mCherry/+ heterozygous flies derived from the same cross were used to generate control embryos for this experiment. *dlg1*² is a temperature-sensitive allele that shows progressively worse phenotypes from 18°C to 29°C, whereas *dlg1*⁵ is a hypomorphic allele that is weakly temperature sensitive (Perrimon, 1988). Both control and *dlg1*²/*dlg1*⁵ embryos were imaged for Utr-Venus at 22°C.

For optogenetic disruption of F-actin, females from the UASp-pmCIBN/FM6; UASp-CRY2-OCRL/TM3 stock were crossed to Mat67 Sqh-mCherry; Mat15 E-cad-GFP/TM3 males to generate UASp-pmCIBN/+ or Y; Mat67 Sqh-mCherry/+; Mat15 E-cad-GFP/UASp-CRY2-OCRL flies.

Embryos derived from these flies were used to determine the effect of stimulation on ventral furrow invagination. To confirm the loss of cortical actin upon stimulation, females from the UASp-pmCIBN/FM6; UASp-CRY2-OCRL/TM3 stock were crossed to Mat67 Sqh-mCherry; Mat15 Utr-Venus/TM3 males to generate UASp-pmCIBN/+ or Y; Mat67 Sqh-mCherry/+; Mat15 Utr-Venus/UASp-CRY2-OCRL flies. Embryos derived from these flies were used in this analysis.

Immunostaining

Mat67 Sqh-mCherry/+; Mat15 E-cad-GFP/*dlg1* TRiP (*dlg1* RNAi) and Mat67 Sqh-mCherry/+; Mat15 E-cad-GFP/+ (control) flies were kept at 18°C and embryos were collected from overnight plates. Embryos were dechorionated with bleach for 1 min, collected with a metal mesh, and rinsed extensively. Embryos were subsequently fixed with 10% paraformaldehyde for 1 h. Following removal of the vitelline membrane, embryos were blocked with 10% bovine serum albumin (BSA) in PBS and 0.1% Tween 20. Primary antibody staining for Dlg1 (1:50; mouse, Developmental Studies Hybridoma Bank, 4F3 anti-discs large) and GFP (1:500; rabbit, EMD Millipore, AB3080P) was carried out in PBT (PBS/0.1% BSA/0.1% Tween 20) overnight at 4°C. Secondary antibody staining with Alexa Fluor 488 (1:500; anti-mouse; Invitrogen, A11029) and Alexa Fluor 568 (1:500; anti-rabbit; Invitrogen, A11036) was carried out at room temperature for 1 h. Nuclei were stained with DAPI (Sigma-Aldrich, D9542; 1:10) for 3 min at room temperature. Embryos were mounted on glass slides containing Aqua Polymount (Polysciences). An A1 Nikon Confocal microscope with a 40× oil objective and 405 nm, 488 nm and 568 nm lasers was used for imaging. Image size was 1024 pixels×1024 pixels (0.21 μm/pixel).

Confocal live imaging of ventral furrow formation and data analysis

All live imaging was performed at room temperature. Embryos were dechorionated in 40% bleach (~3% sodium hypochlorite), rinsed thoroughly with water, transferred onto a 35 mm MatTek glass-bottom dish (MatTek Corporation), and covered with water. In order to screen for invagination mutants, live imaging of control and RNAi embryos expressing a GFP-tagged junctional/membrane marker, E-cadherin, and an mCherry tagged myosin marker, Spaghetti Squash, was performed using a Zeiss Axio Observer laser scanning confocal microscope (LSM 880), a 40×/1.3 numerical aperture oil-immersion objective, a 488 argon laser and a 561 laser. A 1.57× zoom was used. Nine to eleven confocal z-sections with a step size of 1 μm were acquired, with a temporal resolution ranging from 11 to 22.5 s. We focused on a relatively shallow region near the surface of the ventral tissue so that we could analyze apical cell dynamics with relatively high spatial and temporal resolution. The image size was 512 pixels×512 pixels, which corresponds to a lateral pixel size of 265 nm. The total imaged size was approximately 136 μm×136 μm. The analyses of the confocal data are described below. All quantification and data plotting were performed using MATLAB (MathWorks), R, or Microsoft Excel, unless otherwise stated.

Analysis of tissue flow during ventral furrow formation

To measure tissue flow at the ventral surface of the embryo during ventral furrow formation (Fig. 1), cartographic distortion due to the curvature of the embryo surface was corrected by generating a flattened surface view as described by Heemskerk and Streichan (2015). Particle image velocimetry (PIV) software (OpenPIV) (Taylor et al., 2010) was used to track the tissue movement towards the ventral midline from the surface view. A spacing/overlap of 32 pixels×32 pixels and an interrogation window size of 32 pixels×32 pixels was used. The average velocity of tissue movement towards the ventral midline (V_x) was defined as the average velocity along the medial-lateral (ML) axis (the x direction under the described imaging setting) within a region 10–30 μm away from the ventral midline. Embryos were aligned in time based on the initial increase in V_x during apical constriction.

Quantification of the rate of apical constriction

To confirm that apical constriction was normal in the *dlg1* RNAi embryos (Fig. 1H–J), individual constricting cells were segmented from the surface

view of the movies using Embryo Development Geometry Explorer (EDGE), a MATLAB-based image segmentation tool (Gelbart et al., 2012). E-cadherin-GFP was used as a membrane marker. EDGE detects membranes and fits individual cells into polygons. Manual corrections were carried out to ensure individual cells were segmented properly. The apical areas of individual cells within the constriction domain were traced 1–2 min before the onset of apical constriction and onwards until they disappeared from the surface view. The rate of constriction for individual cells was calculated as the rate of area reduction during the course of apical constriction. Four control embryos and four representative *dlg1* RNAi embryos were analyzed.

Quantification of the extent of flanking cell stretching

To determine the cell aspect ratio of the flanking cells (Fig. 4), flanking cells at T_{trans} were segmented from the apical surface view using EDGE. The areas of the segmented cells were measured. To obtain the aspect ratio of the cell, each segmented cell was fitted to an ellipse using the ‘fit_ellipse’ function in MATLAB. Next, the intersection between the long or short axis of the fitted ellipse and the segmented cell boundary was determined and used as a measurement for the long or short axis of the cell, respectively. The aspect ratio of the cell was defined as the ratio between the long axis and the short axis of the cell.

Analysis of myosin pulses in the flanking cells

To quantify apical myosin activity in the flanking cells and analyze its impact on apical cell shape dynamics (Fig. 5), we segmented the apical domain of individual flanking cells and measured apical myosin intensity over time. A z-plane close to the apical myosin signal was selected, and the E-cadherin-GFP signal was used to segment the cell outlines over time using EDGE. We focused our analysis between 4 min before T_{trans} and 2 min after T_{trans} (approximately 4–10 min after the onset of apical constriction), when myosin coalescence was most frequently observed in the flanking cells. To select flanking cells, cells were first filtered based on their distance from the ventral midline at T_{trans} (16–40 μm). Flanking cell identity was then manually confirmed based on whether apical stretching was observed during apical constriction. To analyze apical myosin in the embryo, maximum projections of apical Sqh-mCherry signal within 5 μm from the apical surface were generated using the following approach in ImageJ. First, the z-slice with the brightest apical myosin signal at T_{trans} was determined (Z_a). Next, a sub-stack including Z_a and all z-slices 5 μm below Z_a was generated. Next, a Gaussian blur filter with a σ (radius) of 1 (pixel) was applied to each z-slice in the sub-stack to reduce noise. Finally, a maximum intensity projection was generated from the Gaussian-blurred sub-stack. Myosin intensities between different embryos were normalized based on the background apical myosin intensity at a reference time point (T_{ref}) that was <1 min before T_{trans} . Background myosin intensity (Myo_{BG}) was defined as the myosin intensity in regions where no myosin pulses were detected at T_{ref} and was determined as follows. For each embryo, the mean pixel intensity of apical myosin for each segmented cell was measured and plotted as a function of the position of the cell relative to the ventral midline at T_{trans} . The myosin intensities lowered quickly from 0 μm to 15 μm and reached the floor at 20–30 μm. Myo_{BG} was defined as the myosin intensity at the floor. A scaling factor (sf) was then calculated by dividing Myo_{BG} by the mean myosin background intensity of all embryos analyzed. For each embryo, the normalized apical myosin intensity (Myo_{NOR}) for a single segmented cell was calculated as:

$$Myo_{NOR} = (Myo_{TOT} - Myo_{BG} \times N_{pxl}) / sf,$$

where Myo_{TOT} is the total myosin intensity within the apical domain of the cell and N_{pxl} is the size of the apical domain in pixels. For each segmented flanking cell, the normalized apical myosin intensities were plotted over time as a heatmap to reveal cycles of apical myosin accumulation and disappearance.

To analyze myosin pulses in the flanking cells, individual myosin coalescence events were manually identified. For each event, the time point when apical myosin coalesced into a focused, high-intensity punctum was defined as the pulse peak. A 96-s time interval centered around the pulse peak, which we referred to as a myosin ‘pulse’, was used for analysis of

changes in apical cell area, apical cell length and apical myosin intensity. The 96-s interval was selected because it covers the rising and falling phases of myosin intensity during a single coalescence event, meanwhile minimizing overlap between consecutive pulses. To compare cell behaviors during pulses and time intervals between pulses, 96-s intervals centered around time points showing local minimums of myosin intensity were selected as ‘off-pulses’ and analyzed. Off-pulses served as controls for pulses.

To analyze the coupling between myosin coalescence and local cell deformation, the change in the width of the cell along the anterior-posterior direction at the position where myosin coalescence occurred (‘dH’; Fig. 5M) was manually measured in ImageJ. dH was used as a ‘coupling index’ to represent local cell shape change associated with the myosin coalescence. In control flanking cells, there are various degrees of coupling between myosin coalescence and local cell shape deformation. When coupling is strong, myosin coalescence correlates with pulling and bending of the cell-cell boundary towards the center of the apical domain (Fig. 5M). When there is weak or no coupling, no obvious local deformation is observed during myosin coalescence. In control embryos, the apical area of the flanking cells underwent a net reduction during strongly coupled pulses (defined as $dH < -0.8 \mu\text{m}$) and a net increase during weakly coupled pulses (defined as $dH > -0.8 \mu\text{m}$) (Fig. 5N,O). The result is consistent with the expectation that more strongly coupled pulses result in more prominent apical area reduction, which validates the use of dH as the coupling index.

Imaging and analysis of the localization of subapical landmarks

In order to examine the localization of subapical components during polarity establishment, live imaging of control and *dlg1* mutant embryos expressing Canoe-YFP, Bazooka-GFP, E-cadherin-GFP (Fig. S3) or Utraphin-Venus (Fig. S4) was performed with an Olympus FVMPE-RS multiphoton microscope, a 25 \times /1.05 numerical aperture water-immersion objective, and a 920 nm pulsed laser. A 1 \times zoom was used. Single-plane images (1024 pixels \times 1024 pixels, or 509 $\mu\text{m}\times$ 509 μm) at the midsagittal plane of the embryo were acquired in 1-min intervals until germband extension. The lateral pixel size was 0.50 μm . Embryos were mounted lateral side up such that both dorsal and ventral sides of the embryo were captured when imaged at the midsagittal plane. In order to quantify actin distribution along the lateral membrane of the non-constricting ectodermal cells, the image frame corresponding to the onset of ventral furrow formation was selected, and a region of interest (251 pixels \times 93 pixels, 125 $\mu\text{m}\times$ 46 μm) covering approximately 24 epithelial cells at the dorsal region of the embryo was used for quantification. The positions of the lateral membranes were manually segmented by drawing a line along each lateral cortical F-actin signal. Mean Utr-Venus intensity was integrated along each segmented lateral membrane with a width of 5 pixels (2.5 μm). The measured intensity was subsequently normalized between embryos based on the mean signal intensity within the epithelial layer at the dorsal side of the embryo. Between 14 and 24 lateral membranes were measured for each embryo and averaged to determine the apical-basal distribution of cortical actin. Finally, the apical-basal distribution of cortical actin signal in embryos with the same maternal genotype were averaged to generate the mean actin distribution.

Multiphoton-based deep-tissue live imaging and data analysis

Deep-tissue live imaging of ventral furrow formation in control and *dlg1* RNAi embryos was performed with an Olympus FVMPE-RS multiphoton microscope, a 25 \times /1.05 numerical aperture water-immersion objective, and a 920 nm pulsed laser. A 3 \times zoom was used. Embryos were mounted ventral side up. For different batches of experiments, two similar acquisition conditions were used. In the first condition, stacks of 51 images taken at 2- μm steps were acquired during ventral furrow formation in 2-min intervals with a resonant scanner. A region of interest (512 pixels \times 256 pixels, 170 $\mu\text{m}\times$ 85 μm) that encompassed the mid-region of the embryo (around 50% of egg length) was imaged. In the second condition, stacks of 100 images taken at 1- μm steps were acquired in 2-min intervals with a Galvano scanner. A smaller region of interest, 512 pixels \times 128 pixels (170 $\mu\text{m}\times$ 42 μm), was imaged. In both imaging conditions, laser power was increased linearly over the span of 100 μm in order to compensate for

the loss of signal due to light scattering. The analyses of the multiphoton data are described below.

Measurement of the rate of ventral furrow invagination

To measure the rate of ventral furrow invagination (Fig. 2A-F), cross-section views encompassing the entire depth of the ventral furrow were generated in ImageJ through re-slicing, followed by an average projection of 20 slices. Embryos were aligned by time based on the onset of apical constriction. The rate of furrow ingression was measured by manually tracking the invagination depth, D (i.e. the distance between the vitelline membrane and the apex of the ventral-most cell), over time during ventral furrow formation.

Analysis of the 3D morphology of the ventral furrow at T_{trans}

The following analyses were performed to evaluate the morphology of the intermediate furrow at T_{trans} (defined as 8 min after the onset of apical constriction for multiphoton movies with a 2-min resolution) (Fig. 2G-J). First, the apical and basal arcs of the ventral furrow at T_{trans} were manually outlined from the cross-section view in order to quantify the apical and basal arc length. Second, the furrow thickness was measured by determining the distance between the apical and basal membranes of the cells closest to the ventral midline. Finally, a single row of cells encompassing the constriction domain and the flanking cells were segmented in 3D using EDGE and the surfaces of the segmented cells were plotted in 3D for comparison.

Analysis of mesodermal and ectodermal cell movement during ventral furrow formation

To analyze the ventrally directed movement of the non-constricting cells towards the ventral midline during ventral furrow formation (Fig. 6), a flattened ventral surface view was generated from each multiphoton movie using a custom MATLAB script. A row of \sim 12 cells on one side of the ventral midline that included approximately six constricting cells, three flanking cells and approximately three ectodermal cells was segmented from the surface view using EDGE and manually tracked over time. Quantities, such as apical cell area, the M-L position of the cell apex, and the distance traveled to the midline, were extracted from the segmented cells. The measurements were further interpolated based on the initial M-L position of the cells at the onset of apical constriction and subsequently averaged between embryos from the same genotype. The velocity of cell movement between 0 and 8 min was calculated based on the measurement of cell position over time.

Magnetic tweezers

Embryos were dechorionated and mounted ventral side down on a 24 mm \times 50 mm 1.5 coverslip containing a thin layer of glue on the surface. Once mounted, the embryos were dried in a desiccator for 12 min. After desiccation, embryos were covered with a 3:1 mixture of 700/27 halocarbon oil. Yellow fluorescent carboxyl magnetic particles, 0.5 μm in diameter (Spherotech), were diluted in water (1:10) and injected into the periplasm of the embryos during cellularization using a FemtoJet express microinjector (Eppendorf). The embryos used in this experiment expressed Utr-Venus and Sqh-mCherry which allowed us to monitor cell shape and actomyosin dynamics. A custom-built electromagnet was used to pull on the magnetic beads.

Before each experiment, a z-stack spanning approximately one-third of the thickness of the embryo, taken at 1- μm steps, was acquired to record the distribution of magnetic beads within the embryo. Simultaneous dual-color imaging was performed with an inverted Nikon spinning disk confocal Ti microscope, a 488 nm laser, a 561 nm laser and a 40 \times oil-immersion objective. Images are 2048 pixels \times 2048 pixels (340 $\mu\text{m}\times$ 340 μm). The lateral pixel size is 166 nm. The total intensity of beads within each embryo was determined by subtracting the background levels of fluorescence from the total image intensity. Because the magnetic beads were much brighter than Utr-Venus, the presence of Utr-Venus in the embryos did not noticeably affect the quantification of the intensity of the beads.

To capture the response of the magnetic beads to pulling from the electromagnet, simultaneous dual-color imaging was performed with a Nikon spinning disk confocal Ti microscope, a 488 nm laser, a 561 nm laser

and a 40 \times oil-immersion objective. Images 2048 pixels \times 2048 pixels (340 μ m \times 340 μ m) in size were acquired at a single focal plane within the periplasm every 0.43 s. After image acquisition, the displacement of the magnetic beads along the direction of pulling was manually tracked over time. Three clusters of magnetic beads near the center of the bead distribution were chosen for manual tracking. The position of a group of cells away from the clusters of magnetic beads was measured as a control. In some instances, embryos were slightly rotated within the eggshell upon pulling. Embryo rotation was detected when cells located far away from the beads (the ‘control cells’) moved in the direction of pulling as a cohort without showing obvious local cell shape changes. To account for this global movement, we generated rotation-corrected displacement curves by subtracting the displacement of the control cells from that of the magnetic beads. For each embryo, the average bead displacement curve was generated from the displacement curves of three clusters of manually tracked beads. The displacement curves include displacement of the beads during the resting phase (60 s), the pulling phase (30 s) and the recovery phase (\sim 120 s). The maximum displacement of the beads was set as the total bead displacement during the entire pulling phase. The percentage recovery of the beads was calculated by dividing the net displacement of beads during the first 100 s of the recovery phase by the total displacement of the beads during the pulling phase.

Laser ablation of the flanking cells

Embryos expressing E-cadherin-GFP were prepared in the same way as for regular live imaging described above. Embryos were mounted ventral side up and imaged with an Olympus FVMPE-RS multiphoton microscope, a 25 \times /1.05 numerical aperture water-immersion objective, a 920 nm pulsed laser and a Galvano scanner. A 3 \times zoom was used. For each laser-ablation experiment, an embryo at the mid-phase of apical constriction was selected, and the following three steps were repeated for 30 cycles. In the first step, z-stacks of 21 images taken at 2- μ m steps were acquired for two time points in 8-s intervals, for a total of 16 s. Images encompass the apical region of the embryo and are 512 pixels \times 128 pixels (170 μ m \times 42 μ m) in size. In the second step, laser ablation of one strip of flanking cells 50 pixels \times 250 pixels in size (17 μ m along the medial-lateral axis and 83 μ m along the anterior-posterior axis) was performed on both sides of the constriction domain. Laser ablation was performed for 2 s on the apical-most domain of the flanking cells and spanned a depth of 2 μ m. To avoid any adverse effects from wound healing responses, the laser power was carefully tuned such that no visible damage on the plasma membrane was observed after laser ablation (evidenced by prompt recovery of the plasma membrane signal of E-cadherin-GFP after laser ablation; Fig. 7C). However, we cannot confidently conclude that the plasma membrane remains completely intact, as there could have been damage that was not detectable under the imaging conditions we used. The effectiveness of this ablation approach was confirmed by treating tissues that were under tension. After laser ablation, the surrounding tissues immediately retracted from the ablated site, an expected tissue response when the mechanical integrity of a laser-treated region is disrupted (Fig. 7C). The third step was similar to the first step, except that six time points were acquired for a total of 48 s. The total length of duration for all three cycles was 68 s, and for 30 iterations it took approximately 35 min. In this protocol, the flanking cells were subjected to laser ablation for 2 s every 68 s. We found that repeating laser ablation was necessary to prevent active shrinking of the cut apical domain, which typically happened \sim 1 min after cutting. A similar protocol was used for the control experiments, except that a much lower laser power was used in step 2, such that only photobleaching occurred and there was no visible recoil indicative of laser ablation.

After image acquisition, cross-section views were generated in ImageJ by re-slicing, followed by an average intensity projection of 20 slices. In addition, ventral surface views were generated from the original image stacks using a custom MATLAB script. The rate of ventral furrow invagination was manually tracked from the cross-section view by measuring the invagination depth, D , over time after laser ablation. Embryos were aligned in time by T_{trans} in order to compare the rate of invagination.

Optogenetic disruption of cortical F-actin

Embryos were prepared in the same way as for regular live imaging, except that the preparation was performed either in the dark or under red light. Single-color imaging was performed with an Olympus FVMPE-RS multiphoton microscope, a 25 \times /1.05 numerical aperture water-immersion objective, a 1040 nm laser line and a resonant scanner. A 3 \times zoom was used. Stacks of 101 images taken at 1- μ m steps were acquired in 1-min intervals before and after optogenetic stimulation. Images encompassed the mid-region of the embryo (around 50% of the egg length) and were 512 pixels \times 512 pixels (170 μ m \times 170 μ m) in size. Because it took significantly longer to disrupt the flanking cells with optogenetics than with laser ablation, it was technically more challenging to target the flanking cells on both sides of the constriction domain reliably. We therefore performed stimulation in the flanking cells on one side of the constriction domain. For optogenetic stimulation, a single apical plane within the selected region of interest encompassing a stripe of flanking cells (170 μ m along the anterior-posterior axis) was scanned (with Galvano scanning) for about 2 min using the 920 nm laser. Images before and after stimulation were acquired using the 1040 nm laser. Stimulation was performed during apical constriction. We first tested stimulating a 170 μ m \times 10 μ m rectangular region that spanned one column of flanking cells. Unexpectedly, the treatment resulted in only minor effects on invagination, perhaps owing to relatively mild disruption of the flanking cells. We then increased the width of the stimulated area to \sim 30 μ m, which spanned four or five columns of non-constricting cells next to the constriction domain. The stimulated region included the flanking cells and one or two rows of ectodermal cells at one side of the constriction domain. Embryos with an identical maternal genotype but imaged without stimulation were used as control for this experiment. Cross-section views were generated in ImageJ. Ventral surface views were generated from the original image stacks using a custom MATLAB script. The alignment of time and the rate of ventral furrow ingression was determined in the same way as in the laser-ablation experiments.

Statistical analysis

Sample sizes for the presented data and methods for statistical comparisons are given in figure legends. P -values were calculated using MATLAB `ttest2` or `ranksum` functions.

Acknowledgements

We thank A. Lavanway for help with imaging and research support in general; B. Robertson for help with building the electromagnet used in our experiments; B. J. Gurgeot and K. P. Royce for help with pilot data analysis; S. De Renzis and Y. C. Wang for sharing reagents; E. Griffin and J. Moseley for their valuable feedback on our manuscript; M. Peifer and T. Bonello for helpful discussion; the B.H. lab members for constructive comments and discussions; and the Bloomington *Drosophila* Stock Center and the Developmental Studies Hybridoma Bank for providing reagents used in this work.

Competing interests

The authors declare no competing or financial interests.

Author contributions

Conceptualization: M.A.F., B.H.; Methodology: M.A.F., B.H.; Software: M.A.F., B.H.; Validation: M.A.F., B.H.; Formal analysis: M.A.F., B.H.; Investigation: M.A.F.; Resources: B.H.; Data curation: M.A.F.; Writing - original draft: M.A.F.; Writing - review & editing: M.A.F., B.H.; Visualization: M.A.F., B.H.; Supervision: B.H.; Project administration: B.H.; Funding acquisition: B.H.

Funding

This research was supported by a National Institute of General Medical Sciences ESI-MIRA award (R35GM128745 to B.H.) and an American Cancer Society research grant (IRG-16-191-33 to B.H.), and the GAANN fellowship (from the US Department of Education) and the Ryan fellowship (from the Albert J. Ryan Foundation) to M.A.F. Deposited in PMC for release after 12 months.

References

- Barrett, K., Leptin, M. and Settleman, J. (1997). The Rho GTPase and a putative RhoGEF mediate a signaling pathway for the cell shape changes in *Drosophila* gastrulation. *Cell* **91**, 905-915. doi:10.1016/S0092-8674(00)80482-1
- Bilder, D., Li, M. and Perrimon, N. (2000). Cooperative regulation of cell polarity and growth by *Drosophila* tumor suppressors. *Science* **289**, 113-116. doi:10.1126/science.289.5476.113

- Bonello, T. T., Choi, W. and Peifer, M. (2019). Scribble and Discs-large direct initial assembly and positioning of adherens junctions during the establishment of apical-basal polarity. *Development* **146**, dev180976. doi:10.1242/dev.180976
- Costa, M., Wilson, E. T. and Wieschaus, E. (1994). A putative cell signal encoded by the folded gastrulation gene coordinates cell shape changes during *Drosophila* gastrulation. *Cell* **76**, 1075-1089. doi:10.1016/0092-8674(94)90384-0
- Dawes-Hoang, R. E., Parmar, K. M., Christiansen, A. E., Phelps, C. B., Brand, A. H. and Wieschaus, E. F. (2005). folded gastrulation, cell shape change and the control of myosin localization. *Development* **132**, 4165-4178. doi:10.1242/dev.01938
- Denk-Lobnig, M., Totz, J. F., Heer, N. C., Dunkel, J. and Martin, A. C. (2021). Combinatorial patterns of graded RhoA activation and uniform F-actin depletion promote tissue curvature. *Development* **148**, dev199232. doi:10.1242/dev.199232
- Fuse, N., Yu, F. and Hirose, S. (2013). Gprk2 adjusts Fog signaling to organize cell movements in *Drosophila* gastrulation. *Development* **140**, 4246-4255. doi:10.1242/dev.093625
- Gelbart, M. A., He, B., Martin, A. C., Thiberge, S. Y., Wieschaus, E. F. and Kaschube, M. (2012). Volume conservation principle involved in cell lengthening and nucleus movement during tissue morphogenesis. *Proc. Natl. Acad. Sci. USA* **109**, 19298-19303. doi:10.1073/pnas.1205258109
- Gracia, M., Theis, S., Proag, A., Gay, G., Benassayag, C. and Suzanne, M. (2019). Mechanical impact of epithelial-mesenchymal transition on epithelial morphogenesis in *Drosophila*. *Nat. Commun.* **10**, 2951. doi:10.1038/s41467-019-10720-0
- Guglielmi, G., Barry, J. D., Huber, W. and De Renzis, S. (2015). An optogenetic method to modulate cell contractility during tissue morphogenesis. *Dev. Cell* **35**, 646-660. doi:10.1016/j.devcel.2015.10.020
- Häcker, U. and Perrimon, N. (1998). DRhoGEF2 encodes a member of the Dbl family of oncogenes and controls cell shape changes during gastrulation in *Drosophila*. *Genes Dev.* **12**, 274-284. doi:10.1101/gad.12.2.274
- Heemskerk, I. and Streichan, S. J. (2015). Tissue cartography: compressing bio-image data by dimensional reduction. *Nat. Methods* **12**, 1139-1142. doi:10.1038/nmeth.3648
- Hunter, C. and Wieschaus, E. (2000). Regulated expression of nullo is required for the formation of distinct apical and basal adherens junctions in the *Drosophila* blastoderm. *J. Cell Biol.* **150**, 391-401. doi:10.1083/jcb.150.2.391
- John, A. and Rauzi, M. (2021). A two-tier junctional mechanism drives simultaneous tissue folding and extension. *Dev. Cell* **56**, 1469-1483.e5. doi:10.1016/j.devcel.2021.04.003
- Kerridge, S., Munjal, A., Philippe, J.-M., Jha, A., de las Bayonas, A. G., Saurin, A. J. and Lecuit, T. (2016). Modular activation of Rho1 by GPCR signalling imparts polarized myosin II activation during morphogenesis. *Nat. Cell Biol.* **18**, 261-270. doi:10.1038/ncb3302
- Kim, H. Y., Varnier, V. D. and Nelson, C. M. (2013). Apical constriction initiates new bud formation during monopodial branching of the embryonic chicken lung. *Development* **140**, 3146-3155. doi:10.1242/dev.093682
- Kölsch, V., Seher, T., Fernandez-Ballester, G. J., Serrano, L. and Leptin, M. (2007). Control of *Drosophila* gastrulation by apical localization of adherens junctions and RhoGEF2. *Science* **315**, 384-386. doi:10.1126/science.1134833
- Krueger, D., Tardivo, P., Nguyen, C. and De Renzis, S. (2018). Downregulation of basal myosin-II is required for cell shape changes and tissue invagination. *EMBO J.* **37**, e100170. doi:10.15252/embj.2018100170
- Leptin, M. (1991). twist and snail as positive and negative regulators during *Drosophila* mesoderm development. *Genes Dev.* **5**, 1568-1576. doi:10.1101/gad.5.9.1568
- Leptin, M. (1999). Gastrulation in *Drosophila*: the logic and the cellular mechanisms. *EMBO J.* **18**, 3187-3192. doi:10.1093/emboj/18.12.3187
- Leptin, M. and Grunewald, B. (1990). Cell shape changes during gastrulation in *Drosophila*. *Development* **110**, 73-84. doi:10.1242/dev.110.1.73
- Manning, A. J., Peters, K. A., Peifer, M. and Rogers, S. L. (2013). Regulation of epithelial morphogenesis by the G protein-coupled receptor mist and its ligand fog. *Sci. Signal.* **6**, ra98. doi:10.1126/scisignal.2004427
- Martin, A. C. and Goldstein, B. (2014). Apical constriction: themes and variations on a cellular mechanism driving morphogenesis. *Development* **141**, 1987-1998. doi:10.1242/dev.102228
- Martin, A. C., Kaschube, M. and Wieschaus, E. F. (2009). Pulsed contractions of an actin-myosin network drive apical constriction. *Nature* **457**, 495-499. doi:10.1038/nature07522
- Martin, A. C., Gelbart, M., Fernandez-Gonzalez, R., Kaschube, M. and Wieschaus, E. F. (2010). Integration of contractile forces during tissue invagination. *J. Cell Biol.* **188**, 735-749. doi:10.1083/jcb.200910099
- Mason, F. M., Tworoger, M. and Martin, A. C. (2013). Apical domain polarization localizes actin-myosin activity to drive ratchet-like apical constriction. *Nat. Cell Biol.* **15**, 926-936. doi:10.1038/ncb2796
- Morin, X., Daneman, R., Zavortink, M. and Chia, W. (2001). A protein trap strategy to detect GFP-tagged proteins expressed from their endogenous loci in *Drosophila*. *Proc. Natl. Acad. Sci. USA* **98**, 15050-15055. doi:10.1073/pnas.261408198
- Munjal, A. and Lecuit, T. (2014). Actomyosin networks and tissue morphogenesis. *Development* **141**, 1789-1793. doi:10.1242/dev.091645
- Ni, J.-Q., Zhou, R., Czech, B., Liu, L.-P., Holderbaum, L., Yang-Zhou, D., Shim, H.-S., Tao, R., Handler, D., Karpowicz, P. et al. (2011). A genome-scale shRNA resource for transgenic RNAi in *Drosophila*. *Nat. Methods* **8**, 405-407. doi:10.1038/nmeth.1592
- Nikolaïdou, K. K. and Barrett, K. (2004). A Rho GTPase signaling pathway is used reiteratively in epithelial folding and potentially selects the outcome of Rho activation. *Curr. Biol.* **14**, 1822-1826. doi:10.1016/j.cub.2004.09.080
- Nishimura, T., Honda, H. and Takeichi, M. (2012). Planar cell polarity links axes of spatial dynamics in neural-tube closure. *Cell* **149**, 1084-1097. doi:10.1016/j.cell.2012.04.021
- Parks, S. and Wieschaus, E. (1991). The *Drosophila* gastrulation gene *concertina* encodes a Gα-like protein. *Cell* **64**, 447-458. doi:10.1016/0092-8674(91)90652-F
- Perez-Mockus, G., Mazouni, K., Roca, V., Corradi, G., Conte, V. and Schweisguth, F. (2017). Spatial regulation of contractility by Neuralized and Bearded during furrow invagination in *Drosophila*. *Nat. Commun.* **8**, 1594. doi:10.1038/s41467-017-01482-8
- Perrimon, N. (1988). The maternal effect of lethal(1)discs-large-1: a recessive oncogene of *Drosophila melanogaster*. *Dev. Biol.* **127**, 392-407.
- Polyakov, O., He, B., Swan, M., Shaevitz, J. W., Kaschube, M. and Wieschaus, E. (2014). Passive mechanical forces control cell-shape change during *Drosophila* ventral furrow formation. *Biophys. J.* **107**, 998-1010. doi:10.1016/j.bpj.2014.07.013
- Rauzi, M., Lenne, P.-F. and Lecuit, T. (2010). Planar polarized actomyosin contractile flows control epithelial junction remodelling. *Nature* **468**, 1110-1114. doi:10.1038/nature09566
- Roh-Johnson, M., Shemer, G., Higgins, C. D., McClellan, J. H., Werts, A. D., Tulu, U. S., Gao, L., Betzig, E., Kiehart, D. P. and Goldstein, B. (2012). Triggering a cell shape change by exploiting preexisting actomyosin contractions. *Science* **335**, 1232-1235. doi:10.1126/science.1217869
- Royou, A., Sullivan, W. and Karess, R. (2002). Cortical recruitment of nonmuscle myosin II in early syncytial *Drosophila* embryos: its role in nuclear axial expansion and its regulation by Cdc2 activity. *J. Cell Biol.* **158**, 127-137. doi:10.1083/jcb.200203148
- Sawyer, J. K., Harris, N. J., Slep, K. C., Gaul, U. and Peifer, M. (2009). The *Drosophila* afadin homologue Canoe regulates linkage of the actin cytoskeleton to adherens junctions during apical constriction. *J. Cell Biol.* **186**, 57-73. doi:10.1083/jcb.200904001
- Sawyer, J. M., Harrell, J. R., Shemer, G., Sullivan-Brown, J., Roh-Johnson, M. and Goldstein, B. (2010). Apical constriction: a cell shape change that can drive morphogenesis. *Dev. Biol.* **341**, 5-19. doi:10.1016/j.ydbio.2009.09.009
- Sherrard, K., Robin, F., Lemaire, P. and Munro, E. (2010). Sequential activation of apical and basolateral contractility drives ascidian endoderm invagination. *Curr. Biol.* **20**, 1499-1510. doi:10.1016/j.cub.2010.06.075
- Sweeton, D., Parks, S., Costa, M. and Wieschaus, E. (1991). Gastrulation in *Drosophila*: the formation of the ventral furrow and posterior midgut invaginations. *Development* **112**, 775-789. doi:10.1242/dev.112.3.775
- Tanentzapf, G. and Tepass, U. (2003). Interactions between the crumbs, lethal giant larvae and bazooka pathways in epithelial polarization. *Nat. Cell Biol.* **5**, 46-52. doi:10.1038/ncb896
- Taylor, Z. J., Gurka, R., Kopp, G. A. and Liberzon, A. (2010). Long-Duration Time-Resolved PIV to Study Unsteady Aerodynamics. *IEEE Trans. Instrum. Meas.* **59**, 3262-3269. doi:10.1109/TIM.2010.2047149
- Woods, D. F., Hough, C., Peel, D., Callaini, G. and Bryant, P. J. (1996). Dlg protein is required for junction structure, cell polarity, and proliferation control in *Drosophila* epithelia. *J. Cell Biol.* **134**, 1469-1482. doi:10.1083/jcb.134.6.1469
- Zhang, X., Jefferson, A. B., Auethavekiat, V. and Majerus, P. W. (1995). The protein deficient in Lowe syndrome is a phosphatidylinositol-4,5-bisphosphate 5-phosphatase. *Proc. Natl. Acad. Sci. USA* **92**, 4853-4856. doi:10.1073/pnas.92.11.4853

